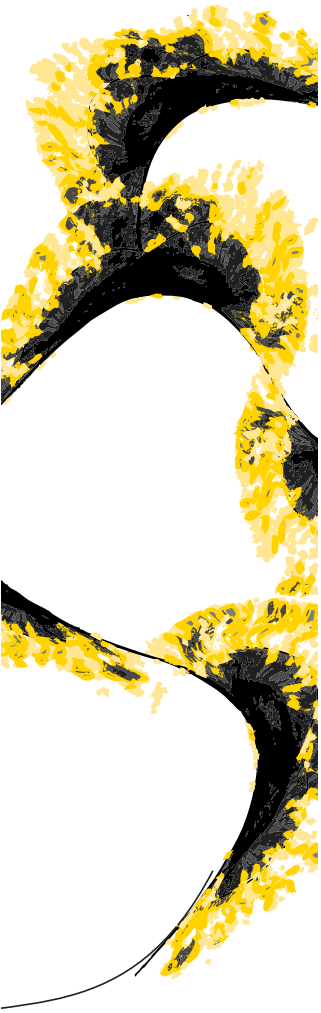

RAM ROBOTICS AND MECHATRONICS

MODELLING AND CONTROL OF UNDERACTUATED FINGER-BASED GRIPPER WITH ADJUSTABLE COMPLIANCE FOR GRASPING OF VARYING AND DEFORMABLE OBJECTS

M. (Mart) Bluiminck

MSC ASSIGNMENT

Committee:
prof. dr. ir. S. Stramigioli
dr. ir. W. Roozing
dr. ir. J.J. de Jong

October, 2022

043RaM2022
Robotics and Mechatronics
EEMCS
University of Twente
P.O. Box 217
7500 AE Enschede
The Netherlands

UNIVERSITY OF TWENTE. | TECHMED CENTRE UNIVERSITY OF TWENTE. | DIGITAL SOCIETY INSTITUTE

Summary

Grasping and manipulation of deformable objects are challenging problems in the food-processing industry, because objects vary widely in size, mass and stiffness. To prevent damaging the object and to secure a stable grasp, this paper proposes a tendon-driven 2-DoF finger-based gripper design with variable joint stiffness utilizing an agonist-antagonist setup. The selected tendon routing configuration obtains independently controllable joint angles and combined joint stiffness while being underactuated. Additionally, a common unactuated degree of freedom realizes a high adaptability for gripper alignment issues and irregular object shapes. An intuitive control strategy is proposed to regulate contact forces at the fingers and regulate stiffness by co-contraction. A proof-of-concept prototype was developed that successfully grasped multiple objects of different size, mass and stiffness. Furthermore, the gripper was capable to increase the joint stiffness by a factor of 3 with less than a 10 % increase in grasp contact force and less than 0.025 rad joint deviation. The prototype showed a joint stiffness range of 0.02-0.48 Nm/rad.

Declaration

I hereby declare that the presented thesis is composed solely by me, M. Bluiminck for the purpose of a graduation thesis as a candidate for the title of MSc. Electrical Engineering. The work presented is my own and has not been submitted for any other degree or professional qualification except the mentioned Msc. title. All work is my own work, except if indicated otherwise. Any findings or work that are not my own contain references to the original author in the bibliography.

Parts of this work may be submitted for publication at a future date.

Preface and Acknowledgements

The research presented is an important personal milestone and is the end of a wonderful journey to obtain the master's degree in Electrical Engineering at the Univeristy of Twente. During this journey, I got acquainted with many interesting friends in the field. I am looking forward to apply the gained knowledge in industry. The achievements I could have never done without the people who supported me.

Firstly, I would like to thank dr.ir. W. Roozing for his continued feedback and excellent guidance during the thesis process. His experience has helped to guide the research more effectively and his critical thinking always provided useful feedback. Secondly, the technical staff at the RAM department of the University of Twente, in particular Q. Sable, for their generous feedback and help in practical considerations of the construction and manufacturing. Lastly, I would like to thank my family and friends who have encouraged and supported me all the way, regardless of what happened.

Contents

1 Introduction

1.1 Context

This project is part of the NWO FlexCRAFT program (NWO/TTW, 2022), a collaboration between multiple Dutch universities and companies, which aims to bring robust perception, world modelling, control, and gripping manipulation technology to the Dutch agri-food sector. The topic of this thesis is part of the gripping and manipulation of deformable objects.

Grasping and manipulation of objects remain the most challenging problems in robotics. Objects needing to be grasped can vary wildly in size, mass, stiffness, surface and other object characteristics, which is especially challenging in the food processing industry. In the food processing industry, improved capabilities are required for a successful grasp with minimal risk of damaging the product. The agricultural environment is highly unstructured, and the operating food products are delicate, easily bruised, adhesive and/or slippery (Wang and Zhang, 2018; Zhang et al., 2020).

Grasping drumsticks and chicken fillets are excellent examples of this fundamental problem. The inter-object variation is significant and the products can be stacked up on assembly lines. This research focuses on these examples, where the approximated product dimensions are depicted in Fig. 1.1. The products have a mass of about 100 to 200 grams. The gripper should in that situation ensure a stable grasp. The food industry is highly repetitive, often consisting of assembly lines, and can easily perform over a million grasps per year for a single object. Additionally, the food industry requires daily cleaning and regular replacement of grippers from a hygiene perspective. We define two types of grasps, enveloping grasping and pinch grasping. Envelope grasping utilizes multiple contact points to enclose the object and to maximize the contact area. Pinch grasping only utilizes a two contact points.

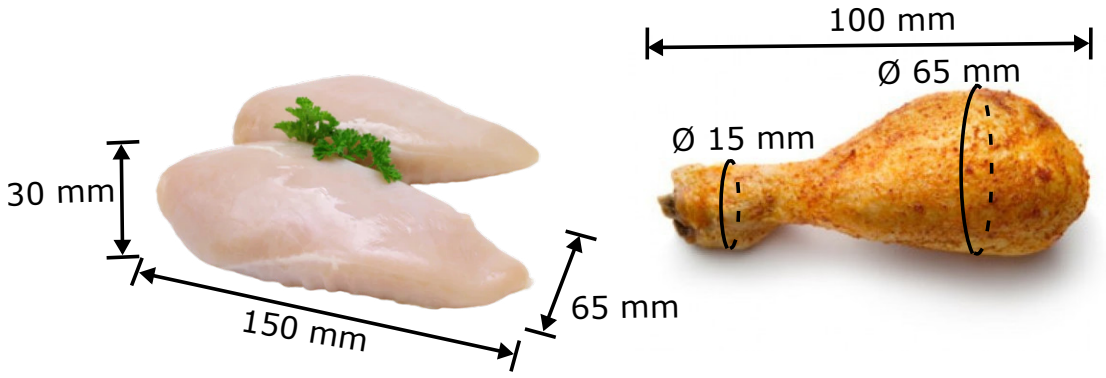

Figure 1.1: Grasp case example. **Left:** Chicken fillets **Right:** Drumstick.

1.2 Problem description

When it comes to grasping irregular and/or fragile objects, rigid grippers may not work as well and even destroy the grasped object. Conventional grippers used in industry have been highly optimized for a single specific grasping object, like the vacuum gripper presented by Sam and Nefti (2010) and the magnetic (fluid) gripper presented by Tsugami et al. (2018). However, air leakage and/or lack of contact area decreases the performance significantly caused by inter-object variation. Also, a higher gripping time is required to carefully set pressures and pressures to prevent product damage (Zhang et al., 2020).

In contrast, humans from a very young age perform complex grasping and manipulation tasks effortlessly; the human hand is a marvel in its complexity, capability, and robustness. Consequently, human hand-inspired finger-based grippers have been widely investigated. By analyzing the grip taxonomy (Cutkosky and Wright, 1986), in most human grasps only two fingers perform a parallel grasp, where the others wrap around the object to increase stability or to perform in-hand manipulation. Reducing the number of fingers is beneficial for the complexity and costs (hygienic replacements). As a result, mainly two and three-finger grippers are considered and in-hand manipulation is outside the scope of this project.

In these human hand-inspired grippers, the muscles are often imitated by tendons routed inside the finger to decrease the gripper's volume and to minimize mass compared to designs with motors at each joint or with 4-bar linkage mechanism as in Tlegenov et al. (2014). The tendons are mostly actuated by electric motors for their simple and precise control ability, their software capabilities and the easy integration of (force)sensors in the food industry (Zhang et al., 2020). The tendon-driven finger-based grippers are investigated in many configurations, fully - / underactuated, with rigid/flexure joints and with passive/active compliance.

Anderson (2011) presented the shadow hand, which showed capabilities approaching the human hand, but with high complexity (129 sensors and 24 DOF). A trade-off is often made between functionality and complexity. More specifically, a repetitive grasp does not require in-hand manipulation or individual degree of freedom (DoF) actuation.

Single actuated tendon-driven (underactuated) designs have been presented such as the 2-finger design (Ciocarlie et al., 2014), 3-finger design (Gao et al., 2020) and 4-finger design (Dollar and Howe, 2009), which showed easy control, adaptability to off-centre gripping and compliance to external forces. The grasp path is limited, which is predefined by the utilization of passive springs/tendons to control the remaining DoFs and to return to the initial pose. Pinch and envelope grasps could be achieved by optimization, but their relatively low load capacity due to intrinsic compliance limits their applications.

Compliant grippers benefit from the characteristic to be adaptive to the shape while grasping. Compliance can be achieved passively or actively. Passive compliance is achieved using rigid bodies and joints with springs to return to the initial position as presented in Dong et al. (2017); Ciocarlie et al. (2014); Rossi and Savino (2014); Ren et al. (2018); Catalano et al. (2014) or with flexible joints as presented in Hussain et al. (2021). With flexible joints, different behaviors, e.g. different fingertip trajectories or fingertip stiffness can be achieved, while keeping the same kinematic structure. Their properties can be adapted e.g. by changing the infill density in a 3D printing process. The flexibility increases the complexity of control and design.

Ren et al. (2018) presented the HERI hand, a tendon-driven 4-finger gripper with passive compliance. Each finger consisting of three bodies was driven by an individual actuator. Consequently, in-hand manipulation and specific tasks like pushing a button are feasible with this configuration. Full sensory feedback of finger modules is provided. Catalano et al. (2014) presented the Pisa/IIT SoftHand hand, a tendon-driven 5-finger gripper with passive compliance. Two actuators move a single tendon from its two sides resulting in two synergies. Firstly, moving both motors in the same direction, the tendon length is shortened and the gripper closes. Secondly, moving the motors in opposite directions slides the tendon without shortening inducing a friction-driven DoA.

The downside of passive compliance is that compliant grippers could neither bear much load nor be controlled precisely due to the compliance of material and structure. Active compliance has the benefit that the grippers stiffness can be adapted in real-time and task-dependent. Additional actuators are required, which increases complexity. Active compliance could be achieved by (de)pressurizing the tendon-driven finger with an enclosed bag filled with air as presented by Gao et al. (2020). However, this stiffness could only be changed when the gripper

is in the final gripping position and a pressure distribution between different bag compartments is required to increase stiffness without changing gripping position.

1.3 Goals and approach

Therefore the question raises:

> "*How can an underactuated tendon-driven gripper be designed, to perform envelope and pinch grasping, of varying and deformable objects, with active adjustable compliance?* "

The main goal is to grasp a variety of objects for an inter-object variation range, which brings a list of desired attractive benefits: (discussed in detail in Chapter 2)

1. Variable joint stiffness / compliant grasping (to prevent damage to product)
2. Dual mode grasping (envelope and pinch grasping)
3. Adaptive grasping (to handle external forces without loosing contact with grasped object)
4. Underactuated (to reduce complexity)
5. Low cost (for regular replacement for hygiene reasons, minimal sensing approach)

The project aims to design a tendon-driven underactuated gripper, where the emphasis is placed on the variable joint stiffness. Initially, a simulation model will be made as a valuable tool for both simulation and development. A two-finger gripper with 2-DoF per finger is proposed. Multiple tendons are routed inside the gripper in series with non-linear springs. The routing is selected to obtain attractive benefits of controllable variables of interest. The other variables of interest are uncontrolled. The non-linear springs can be used to increase joint stiffness by co-contraction in an antagonist-agonist setup. The project includes the fabrication of non-linear springs using a cam-follower design. The aim of the control strategy is to regulate contact forces at the fingers by controlling the non-linear spring deflections. A proof-of-concept will be fabricated using a prototype using rapid prototyping techniques, such as 3D printing and laser cutting. The stiffness range will be determined and the gripper's performance will be evaluated on rigid and deformable objects.

1.4 Outline

The thesis is organized as follows. Firstly, the general requirements are given in Chapter 2 to give an overview of the main goals and contributions of the thesis. It gives motivation why certain requirements are pursued in the final design. This is followed by the core content of the research, which is presented in the paper under Chapter 3. The chapters following the core chapter can be seen as supporting chapters for the main paper. The paper presented the outcome of the design iterations of Chapter 5. Additional findings during the thesis are elaborated in Chapter 4. The paper shortly payed attention to the simulation model, since it is not a core contribution, but rather a tool. Chapter 6 gives discusses further details about the simulation model, including bond-graph model. As the main conclusions have already been presented in the paper, Chapter 7 reflects on the design requirements described in Chapter 2. Details about the screw theory are given in Appendix A.

2 Requirements

As stated above, the main goal is to design a gripper with attractive benefits and to construct a proof-of-concept prototype. Therefore, a MoSCoW for this thesis project is shown below.

- Must have:
  - A novel idea with specific tendon routing, which is able to:
    - change joint stiffness online.
    - perform adaptive grasping (minimize effects induced by gripper alignment issues, irregular object shapes and externally applied forces).
  - A simulation model as a tool for development.
  - Prototype of proof-of-concept.
    - Easy to assemble.
    - Using rapid prototypable techniques.
    - Reasonable range of grasp force and joint stiffness.
- Should have:
  - A (simple) control strategy to regulate contact forces at the fingers.
  - Simulation model as a comparison tool for proof-of-concept prototype.
  - Minimal amount of actuators (underactuation).
  - Includes dual-mode grasping (envelope and pinch).
  - Analysis of key design parameters (attractive benefits).
- Could have:
  - State estimation with remote sensing (of joint 2).
  - Mechanically design optimization (rigidity and compactness).
  - Cost optimization (regular replacement for hygiene, minimal sensing approach).
  - Optimized controller architecture.
  - Analysis and optimization of tendon routing in antagonist-agonist setup.
- Won't have:
  - An in-hand manipulation feature
  - A performance comparison between other grippers in food-industry

For a proof-of-concept, mass and size are subordinate, but should only be fabricated with the available rapid prototypable machines. The specific 3D printer available is the *Ultimaker S5* (Ultimaker, 2022), which provides a build volume of 330mm x 240mm x 300mm. The specific laser cutter is the *Trotec Speedy 300*, which provides a build volume of 400mm x 700 mm and can cut several plastics/wood. As earlier stated, the proposed method for the non-linear spring is a cam-follower using linear springs. The contour, linear-spring stiffness and force-deflection range are coherent design parameters. A stiffer linear spring reduces the slope of the contour and overall size but introduces more non-idealities and measurement errors. Thus a trade-off between size and force-deflection range is explored using the available build volume.

The stiffness range is mainly determined by the range of the force-deflection relation of the non-linear springs. Since the finger's width is minimized to grasp in tight spaces, the moment

arms are limited and high tensile forces are required to apply sufficient torques. It is hard to come up with strict requirements containing stiffness since most designs (utilizing tendons) do not present any information on the stiffness range. The contact grasp force can be compared to the human hand, which ranges from 0.71 N for a pen (≈10 mg) to 14.66 N for a hammer (≈1 kg) (Starke et al., 2019). As earlier defined, the object class of chicken fillets and drumsticks have a mass of about 100 to 200 g. Therefore, the maximum object mass should extend 200 g.

Table 2.1: Overview of quantifiable requirements for prototype.

Parameter	**Amount**	**Unit**
Contact grasp force	0.71 - 14.66	N
Stiffness range	??	Nm/rad
Maximum object mass	≥ 200	g

3 Paper

The following pages show the core of the research, presented as a separate paper which will later possibly be sent for publication.

Modeling and control of underactuated finger-based gripper with adjustable compliance for grasping of varying and deformable objects

Mart Bluiminck, BSc, *m.bluiminck@student.utwente.nl, Electrical Engineering, dept. RaM*

***Abstract*—Grasping and manipulation of deformable objects are challenging problems in the food-processing industry, because objects vary widely in size, mass and stiffness. To prevent damaging the object and to secure a stable grasp, this paper proposes a tendon-driven 2-DoF finger-based gripper design with variable joint stiffness utilizing an agonist-antagonist setup. The selected tendon routing configuration obtains independently controllable joint angles and combined joint stiffness while being underactuated. Additionally, a common unactuated degree of freedom realizes a high adaptability for gripper alignment issues and irregular object shapes. An intuitive control strategy is proposed to regulate contact forces at the fingers and regulate stiffness by co-contraction. A proof-of-concept prototype was developed that successfully grasped multiple objects of different size, mass and stiffness. Furthermore, the gripper was capable to increase the joint stiffness by a factor of 3 with less than a 10% increase in grasp contact force and less than 0.025 rad joint deviation. The prototype showed a joint stiffness range of 0.02-0.48 Nm/rad.**

***Index Terms*—Robotic gripper, Tendon-driven, Variable stiffness, Adaptability, Deformable objects**

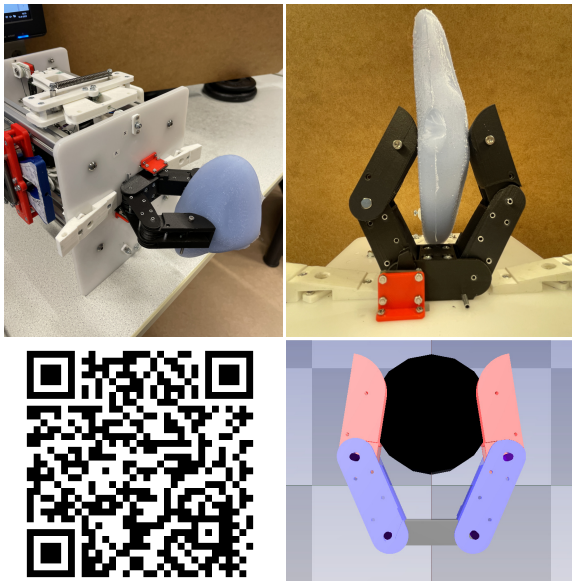

Fig. 1. Simulation model, practical implementation of designed gripper and QR-code to video-footage: www.youtube.com/watch?v=Idmzvgd9JQA.

I. Introduction

Grasping and manipulation of objects remain the most challenging problems in robotics. Objects needing to be grasped can vary wildly in size, mass, stiffness and surface finish. Especially in the food processing industry [1, 2], since products are are delicate, easily bruised, adhesive and/or slippery. In this sector, improved gripper capabilities are needed for a successful grasp with minimal risk of damaging products. Secure grasping not only requires contacting the objects, but also preventing potential slip and damage while the objects are picked and placed [3].

A. State-of-the art grippers in food industry

The food industry has a huge variety of different conventional grippers introduced from other industries to address this issue using electric, pneumatic, magnetic or other actuation types [2]. These grippers are highly optimized for a single object characteristic, e.g. the size, and are used in interchangeable units to deal with the inter-product variation range of a product. This thesis is part of the NWO project FlexCRAFT [4], which aims to bring robust perception, world modelling, control, and gripping manipulation technology to the Dutch agri-food sector.

B. Passive compliant grippers

Compliant grippers benefit from the characteristic to be adaptive to the shape while grasping. Soft robotics based on the fin-ray effect [5] or layer jamming [6] showed a decreased damage risk, high adaptability to off-center gripping and compliance to external force, but could neither bear much load nor be controlled precisely. Specifically, the possible grasp configurations resulting from design optimization are limited and are not online adjustable. Comparable performance and limitations are shown for single actuated rigid-body-based passive-compliant grippers. Those grippers utilize rigid body links in combination with joint springs [7]–[10] or flexible joints [11] to return to the initial position and to passively adapts to the shape of an object. For flexible joints, different behaviors, e.g. different fingertip trajectories or fingertip stiffness can be achieved, while keeping the same kinematic structure. Their properties can be adapted e.g. by changing the infill density in a 3D printing process. The flexibility increases the complexity of control and design.

C. Human-hand inspired grippers

The human hand is well represented as a inspiration source for grippers, since the human hand is marvel in its complexity,

capability and robustness. The muscles are often imitated by tendons routed inside the phalanges as the mechanical transmission system to decrease the gripper's size and weight by locating their actuators remotely from their joints [12]. The 5-finger shadow hand [13] showed comparable capabilities to the human hand, even including in-hand manipulation, but with high (control) complexity of in total 129 force/load sensors and 24 degrees of freedom (DoF). A less complex implementation featuring in-hand manipulation is shown in the 4-finger Heri hand [14]. The Pisa/IIT SoftHand [15], a tendon-driven 5-finger gripper with passive compliance, employs two actuators moving a single tendon from its two ends resulting in two synergies and lower complexity. Muscle synergies have been defined by [16] as patterns of muscle activity whose timing and/or amplitude modulation enable the generation of different movements. In context of tendons, tension exerted on a tendon routed via multiple bodies would generate torques at several joints. Therefore, the motion of multiple joints can occur without the need for multiple tendons resulting in an underactuated system. For the two synergies of the the Pisa/IIT SoftHand, firstly, moving both motors in the same direction, the tendon length is shortened and the gripper closes. Secondly, moving the motors in opposite directions slides the tendon without shortening inducing a friction-driven degrees of actuation (DoA).

D. Active compliant grippers / variable stiffness

All previously mentioned grippers utilize passive compliance which can neither bear much load nor be controlled precisely due to the compliance of material and structure. Active compliance has the benefit that the gripper's joint stiffness can be adapted in real-time and task-dependent. Objects can be approached with high compliance and after a stable grasp equilibrium, the stiffness can be increased to prevent the object from falling out of the gripper by acceleration of the gripper or externally applied forces.

Variable stiffness can be achieved using active impedance control or adaptable inherent compliance [17]. Active impedance control exploits the control loop, which does not allow energy storage and requires a more complex control algorithm compared to inherent compliant mechanisms. Inherent compliance can be achieved by non-linear spring loading (e.g. an agonist-antagonist setup), changing the effective transmission ratio between load and spring [18] and changing physical spring properties. Unlike the other concepts, the latter concept modulates the effective physical structure of a spring [19, 20], e.g. the material modulus (controlled by e.g. temperature) and the cross-sectional area. The control is slow, in case of changing material modulus and/or has no tunable stiffness relation for the cross-sectional area. Next, changing the effective transmission ratio is often complex and requires one actuator for the position and one actuator for the stiffness.

Spring preloading with an agonist-antagonist setup is the simplest method and utilizes two actuators connected to non-linear springs. To obtain adaptable stiffness in an agonist-antagonistic setup, the springs need to be nonlinear [21]. The commercial availability of non-linear springs with a specifiable force-displacement relationship is extremely limited [22], so (adapted) triangle mechanisms [23], four-bar mechanisms [24], and cam-followers [22] have been developed showing strong designed force-displacement behavior in combination with linear springs. All implementations of non-linear spring preloading for grippers have been employed using two actuators for a single joint since both equilibrium and stiffness are independently controlled.

E. Scope and contributions

This work is primarily focused on the design and construction of an underactuated tendon-driven finger-based gripper with key features such as high adaptability and variable joint stiffness. The considered objects are deformable spherical objects with diameters ranging from 25 to 65 mm. This work includes the kinematic analysis of the tendon routing inside grippers. A simulation model is presented as a valuable tool for both simulation and development. The design features are demonstrated in a proof-of-concept prototype. The main contributions can be summarized as follows:

- Novel tendon-driven finger-based gripper design to obtain online adjustable compliance with low design complexity and a limited number of actuators, including mathematical model and parameter exploration.
- Development of a suitable control strategy for contact force control, stiffness regulation, and grasp type control.
- Proof-of-concept prototype (using rapid prototyping techniques) including non-linear springs with designed force-displacement relation.
- Experimental validation of designed gripper, showing key features such as high adaptability and online joint stiffness.

The paper is organized as follows. Firstly, Section II will focus on the analysis of key features. This is followed by Section III which focuses on modelling and simulation of the gripper design and object interaction. Section IV elaborate on the proposed control strategy. Section V presents the mathematical model and fabrication of a non-linear spring with specific force-deflection relation. Section VI focuses on the practical prototype considerations. Section VII presents the gripper key-features validation and design performance. Finally, Sections VIII and IX presents a discussion on the results, a conclusion, highlights possible areas of future work and gives concluding remarks.

II. Concept and analysis

The analysis of the human grip taxomony [25, 26] showed that only two fingers are required for performing a parallel grasp and the other fingers wrap around an object to increase stability. Therefore, a two-finger design is minimal. A minimum number of two phalanges per finger is required to grasp around a spherical object to perform a 5-point stability grasp. Extending the number of phalanges increases the number of stable gripper configurations, while also increasing complexity. Since the goal is a proof-of-concept, the design described from here is a 2-finger 2-DoF per finger parallel gripper as shown in Fig. 2.

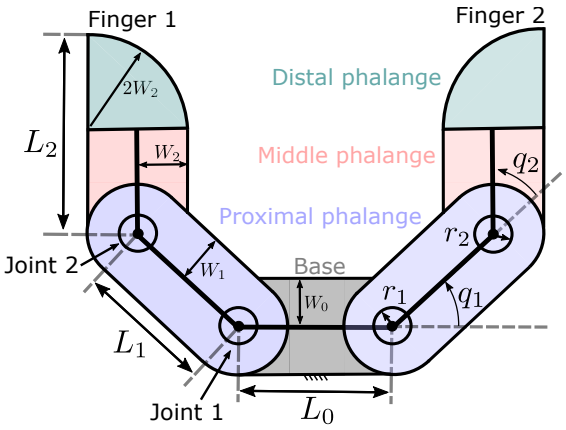

Fig. 2. Kinematic model of 2-DoF per finger gripper. Note that middle and distal phalange are rigidly connected.

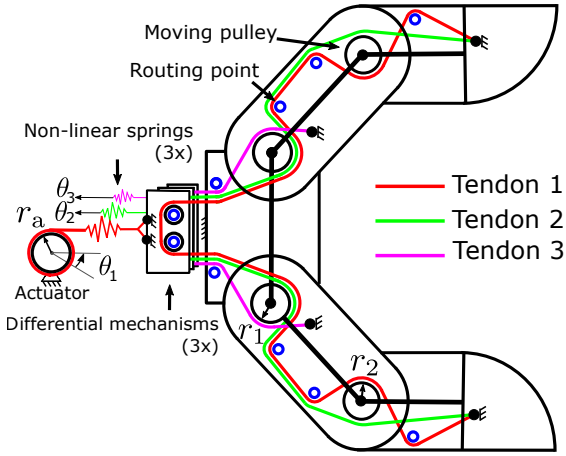

Fig. 3. Kinematic model including actuation scheme and tendon routing.

For a tendon-driven design, the tendon is routed around a joint pulley to apply a joint torque. The tendon-routing highly affects controllability, kinematic motion coupling, and bias forces [27]. Therefore, routing points guide the tendon and ensure contact with the joints. The tendon routing follows an optimal alternating pin allocation [28] resulting in a smooth contact force stabilisation as the fingers achieve a static equilibrium and no sliding occurs.

A. Possible tendon-configurations

Many possible routings exist for tendon-driven designs [27]. The 2-DoF per finger gripper of Fig. 2 has 8 variables of interest, 4 joint angles and 4 corresponding stiffnesses. The tendon routing configuration determines the actively controlled states. The variable joint stiffness feature requires both an actively actuated inside and outside routed tendon around the joint pulleys. Simultaneously, actuating both tendons in opposite directions ensures an independent joint angle enabling envelope and pinch grasping.

Fig. 3 shows the tendon routing inside the gripper. Both tendons around joint 2 are routed via the inside of the first joint, obtaining an independent joint 1 angle state. Actuating both tendons in opposite directions does not affect joint 1 and stiffening of joint 2 results in a closing movement at joint 1. A third tendon compensates for the latter. The result is that both joint angles are independently controlled, while the stiffness of both joints is non-linearly coupled (details in Section III-C).

To prevent containing 6 actuators, the gripper is symmetric and joint angles and stiffnesses of both fingers are coupled, resulting in the other unactuated common mode variables of interest. The latter induces high adaptability.

B. Adaptability

It is beneficial to be adaptable to (object) alignment issues and irregular shapes. Accordingly, a less precise geometry description is required of the object and undesired external contacts effects can be reduced maintaining a stable grasp. Therefore, a differential mechanism is implemented to obtain an unactuated common mode DoF. For symmetric grippers, a review of differential mechanism in the context of grasping are provided [29], presenting three types: gear differentials, linkage whippletree differentials, and pulley differentials.

Raymond *et al.* [30] elaborate on the (dis)advantages, which are listed below. Gear differentials offer compactness at the cost of design complexity and friction, especially when 3D printed. Whippletree differentials utilize the rotation of a bar around a static pivot point to equalize the output difference. The whippletree's compactness and flexibility are limited by its length. It is perfectly suited for 3D printing. Pulley differentials containing a floating or moving pulley offer advantages, since the motion range is not limited like the whippletree. Also, the pulleys could be tracked using small encoders to obtain the tendon displacement. The latter is important since remotely sensing of states is beneficial in the food-processing industry to minimize sensor-object contact (hygiene reasons).

Given these tradeoffs, a double pulley differential is presented as shown in Fig. 3, which combines two horizontally spaced pulleys on a carrier. To prevent rotation of the carrier, the tendon attachment is triangular, with two connection points on the mechanism, since a single attachment would result in a combined whippletree and pulley mechanism, presented in [30]. Moreover, estimating the tendon displacement of the unactuated common mode DoF in a combined whippletree and pulley mechanism would require more than just a single pulley encoder, which would increase complexity.

III. Modelling

A. Generic kinematic model

To obtain the relation of the tendon tension force and the joint torque, the kinematics of tendon-driven mechanism can be established [27]. The following description holds a single finger, but is identical for the other finger since symmetric. For a generic case, with passive and active tendons, the kinematics will be derived. In the following, L, P, N and A represent the number of tendons, passive tendons, joints and actuators, respectively. The kinematic relation between the tendon extension $\boldsymbol{l} \in \mathbb{R}^L$ and the variables such as the joint

angle vector $\boldsymbol{q}$ and the actuator configuration vector $\boldsymbol{\theta}$, can be described as:

$$\boldsymbol{l} = \boldsymbol{l}\left(\boldsymbol{q}, \boldsymbol{\eta}, \boldsymbol{l_0}\right) = \left[\begin{array}{c} \boldsymbol{l}_{\mathrm{a}}(\boldsymbol{q}, \boldsymbol{\theta}) \\ \boldsymbol{l}_{\mathrm{p}}\left(\boldsymbol{q}, \boldsymbol{l}_0\right) \end{array} \right], \tag{1}$$

where $\boldsymbol{l}_{\mathrm{a}}(\boldsymbol{q}, \boldsymbol{\theta})$ and $\boldsymbol{l}_{\mathrm{p}}\left(\boldsymbol{q}, \boldsymbol{l}_0\right)$ are the extensions for active tendon parameters $\boldsymbol{q}, \boldsymbol{\theta}$ and passive tendon parameters $\boldsymbol{q}, \boldsymbol{l}_0$, respectively. $\boldsymbol{l}_0$ denotes the initial extension for the passive tendons. Specifically, $\boldsymbol{q} = (q_1, q_2, \cdots, q_N) \in \mathbb{R}^N$, $\boldsymbol{l_0} = (l_{0,1}, l_{0,2}, \cdots, l_{0,P}) \in \mathbb{R}^P$ and $\boldsymbol{\theta} = (\theta_1, \theta_2, \cdots, \theta_A) \in \mathbb{R}^A$. Moreover, setting $\boldsymbol{J}_{\mathrm{t}}$ to be a Jacobian matrix that maps the joint angle velocity vector $\dot{\boldsymbol{q}}$ to the tendon extension rate $\dot{\boldsymbol{l}}$, the derivative of the tendon extension regarding time can be provided by:

$$\dot{\boldsymbol{l}} = \left[\begin{array}{c} \dot{\boldsymbol{l}}_{\mathrm{a}}(\boldsymbol{q}, \boldsymbol{\theta}) \\ \dot{\boldsymbol{l}}_{\mathrm{p}}\left(\boldsymbol{q}, \boldsymbol{l}_0\right) \end{array} \right] = \boldsymbol{J}_{\mathrm{t}} \dot{\boldsymbol{q}} + \left[\begin{array}{c} \boldsymbol{R}_{\mathrm{a}} \\ 0 \end{array} \right] \dot{\boldsymbol{\theta}}, \tag{2}$$

with the constant jacobian matrix,

$$\boldsymbol{J}_{\mathrm{t}} = \left[\begin{array}{c} \boldsymbol{J}_{\mathrm{a}} \\ \boldsymbol{J}_{\mathrm{p}} \end{array} \right],$$

where $\boldsymbol{J}_{\mathrm{a}} \in \mathbb{R}^{(L-P)\times N}$ and $\boldsymbol{J}_{\mathrm{p}} \in \mathbb{R}^{P\times N}$ are the active and passive Jacobian matrixes, and $\boldsymbol{R}_{\mathrm{a}} \in \mathbb{R}^{A\times A}$ is the diagonal matrix whose diagonal elements are the pulley radii connected with actuators. Using the principle of virtual work, the following expression for the actuation joint torques $\boldsymbol{\tau}_{\mathrm{a}} \in \mathbb{R}^N$ is obtained:

$$\boldsymbol{\tau}_{\mathrm{a}} = -\boldsymbol{J}_{\mathrm{t}}^{\top} \boldsymbol{F}_{\mathrm{t}}, \tag{3}$$

where $\boldsymbol{F}_{\mathrm{t}} \in \mathbb{R}^L$ denotes the vector of tendon tension forces, which is constantly positive since all the tendons cannot generate negative tension force. Since the tension force is just considered, the negative sign is referred to in the above equation.

B. Kinematic model of design

The configuration depicted in Fig. 3 has no passive tendons, three actuators, three tendons, and two joints, $P = 0$, $A = 3$, $L = 3$, $N = 2$, respectively. The wrapping of the tendon around the pulley causes tensile force decrease between tensile force before pulley, T_i, and tensile force after pulley, T_{i+1}, with $T_i \geq T_{i+1}$. The loss is denoted as $0 < \eta_i \leq 1$, such that $T_{i+1} = \eta_i T_i$. The value of η_i is dependent on the type of friction, which is explained in detail in Section III-E. For the specific configuration, $\boldsymbol{F}_{\mathrm{t}}$ can be expressed as:

$$\boldsymbol{F}_{\mathrm{t}} = \left[\begin{array}{ccc} F_{\mathrm{a1}} & F_{\mathrm{a2}} & F_{\mathrm{a3}} \end{array} \right]^{\top}, \tag{4}$$

where $F_{\mathrm{a1}}, F_{\mathrm{a2}}$ and F_{a3} denotes the tensile forces induced by the deflection of the non-linear springs. The jacobian $\boldsymbol{J}_{\mathrm{t}}$ is given by:

$$\boldsymbol{J}_{\mathrm{t}}{}^{\top} = \left[\begin{array}{ccc} -r_1 & -r_1 & r_1 \\ -\eta_1 r_2 & \eta_2 r_2 & 0 \end{array} \right]. \tag{5}$$

From Eq. (3), we can obtain the following equation:

$$\boldsymbol{\tau}_{\mathrm{a}} = \left[\begin{array}{c} \tau_1 \\ \tau_2 \end{array} \right] = - \left[\begin{array}{c} F_{a1} r_1 + F_{a2} r_1 - F_{a3} r_1 \\ \eta_1 F_{a1} r_2 - \eta_2 F_{a2} r_2 \end{array} \right]. \tag{6}$$

In the configuration in Fig. 3, the springs are non-linear following a quadratic force-displacement relation given as:

$$\mathrm{F}(x_i) = a_i \left(x - x_0\right)^2 + b_i \left(x - x_0\right) + c, \tag{7}$$

where the spring deflections x_i for $i = 1, 2, 3$ are given by:

$$\begin{aligned} x_1 &= \theta_1 r_a + q_1 r_1 + q_2 r_2, \\ x_2 &= \theta_2 r_a + q_1 r_1 - q_2 r_2, \\ x_3 &= \theta_3 r_a - q_1 r_1. \end{aligned} \tag{8}$$

If $F(x_1)$ and $F(x_2)$ share the same coefficients, $a_1 = a_2 = a$, $b_1 = b_2 = b$, $c_1 = c_2 = c$ and if the coefficients of $F(x_3)$ equal $a_3 = 2a, b_3 = 2b$ and $c_3 = 2c$, the expression for applied torques τ_1 and τ_2 reduces to:

$$\begin{aligned} \tau_1 = r_1 [& a r_a (\theta_1^2 + \theta_2^2 + 2\theta_3^2) + 2 a q_2^2 r_2^2 + \\ & 2 a r_a q_1 (\theta_1 r_1 + \theta_2 r_1 + 2\theta_3 r_1) + 2 a r_a q_2 (\theta_1 r_2 + \theta_2 r_2) + \\ & b r_a (\theta_1 + \theta_2 - 2\theta_3) + 4 b q_1 r_1] \\ \tau_2 = r_2 [& a r_a^2 (\theta_1^2 - \theta_2^2) + 2 a r_a (\theta_1 q_1 r_1 + \theta_1 q_2 r_2 - \theta_2 q_1 r_1 + \\ & \theta_2 q_2 r_2) + 4 a q_1 q_2 r_1 r_2 + 2 b q_2 r_2 + b r_a (\theta_1 - \theta_2)], \end{aligned} \tag{9}$$

resulting in an intuitive stiffness relation.

C. Stiffness

Stiffness is defined as the rate of change of torque (or force) over (rotational) displacement:

$$k = \frac{\mathrm{d}\tau}{\mathrm{d}q}. \tag{10}$$

The stiffness of joint 1 and joint 2, respectively k_1 and k_2 are calculated using Eqs. (9) and (10), resulting in:

$$\begin{aligned} k_1 &= 2 a r_a r_1^2 (\theta_1 + \theta_2 + 2\theta_3) + 4 b r_1^2 \\ k_2 &= 2 a r_a r_2^2 (\theta_1 + \theta_2) + 4 a q_1 r_1 r_2^2 + 2 b r_2^2 \end{aligned} \tag{11}$$

In this case, both stiffnesses are linearly dependent on co-contraction (i.e., the sum of θ_1 and θ_2 (and θ_3 for k_1), with a constant offset proportional to b. Note that the specific choice of $2a_1 = 2a_2 = a_3 = 2a$, $2b_1 = 2b_2 = b_3 = 2b$ and $2c_1 = 2c_2 = c_3 = 2c$ result, that k_1 is independent of angle q_1, but with a doubled constant offset dependent on b. The offset b is desired to be non-zero, to prevent zero stiffness at zero spring deflection. Moreover, in the fabrication process, (non-linear) springs with constant offset approaching zero are hard to obtain.

D. State estimation with remote sensing

Reducing the number of sensors or locating the sensors remotely reduces possible contact, cleanability and cost. To estimate contact forces without force sensors on each contact point, the state of the gripper is necessary. In the closed tendon system of Fig. 3, assuming no tensile-force induced tendon stretch, the state of joint 2 (q_2), can be reconstructed using the first joint angle (q_1), displacement of differential mechanism routing the first tendon (l_1) and displacement of tendon 1 within the differential mechanism. Since, the differential mechanism guide the tendon over two pulleys, the

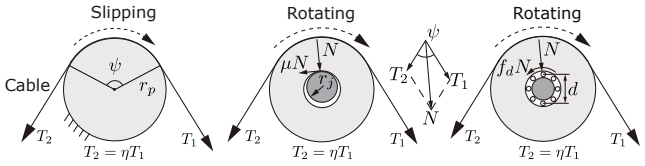

Fig. 4. Friction effects for different routing methods. Image based on [32].

relative displacement is therefore given by its radius (r_4) and angular displacement (q_4). The equality describing lengths is given by:

$$r_1 q_1 + r_2 q_2 = l_1 - r_1 q_4. \tag{12}$$

Assuming equal radii ($r_1 = r_2 = r_4 = r$). The state of joint 2 (q_2) is given by:

$$q_2 = \frac{l_1 - r q_4}{r} - q_1. \tag{13}$$

Similarly, the expression for tendon 2 can be established. The advantage is that the joint 2 encoder can be located in the wrist of the gripper.

E. Friction model

Tendon-driven grippers have little mass and inertia in the phalanges. High tensile forces are necessary to produce significant applied joint torques since the pulley radii size is limited to the phalange width. Hence, the phalange width is limited to allow a compact design for grasping in tight spaces e.g. stacked objects. The pulley radii determine the moment arm for the applied tensile force. Consequently, friction effects may become dominant for high tensile forces.

An important aspect is the effects of the tendon routing inside the gripper. The tendons are routed with fixed routing points on the bodies and pulleys at the joints. The routing points ensure contact of the tendon with the pulleys while grasping, keeping the moment arms of the applied tensile forces constant. The routing points reduce the tensile force due to wrapping friction. The optimal configuration, based on grasp stability and tensile force efficiency utilizes an alternating pin allocation [28, 31].

Pulleys can be implemented in different ways, by 1) a tendon slipping over a fixed pulley, 2) a bushing-supported pulley or 3) a bearing-supported pulley as indicated in Fig. 4. Case 1 is applicable for the routing points inside the phalanges, where the tendons slip around a fixed pulley since space is limited. Cases 2 and 3 have different friction effects.

As earlier stated in Section III-B, friction causes the tension force to decrease when it wraps around pulleys and/or routing points, $T_{i+1} = \eta_i T_i$. To find a expression of η_i (same as in Eq. (6)), η_i is given for slipping by [32]:

$$\eta_i = e^{-\mu\theta}, \tag{14}$$

with friction coefficient μ and contact angle around pulley ψ. For a bushing-supported and bearing-supported pulley, η_i is instead given by [32]:

$$\eta_i = \frac{\alpha^2 + \cos(\psi) - \sqrt{(1+\cos(\psi))\,(2\alpha^2 + \cos(\psi) - 1)}}{\alpha^2 - 1}. \tag{15}$$

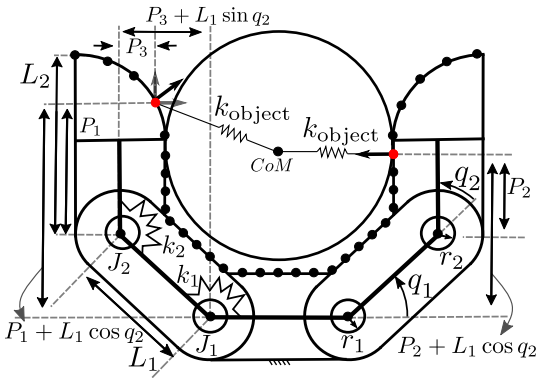

Fig. 5. Contact model. A finite number of contact points are shown as black dots along the gripper surface. Each contact point is connected via a 'fictitious' spring to the center of mass of the object, indicated for the two red dots.

with $\alpha = r_{\text{p}}/(\mu r_{\text{j}})$ for a journal bearing and with $\alpha = r_{\text{p}}/(f_{\text{d}} d)$ for a rolling bearing, where f_{d} is the friction moment coefficient similar to μ, and d is the diameter of the rolling bearing, as indicated in Fig. 4. The derivation assumes negligible pulley inertia, no slipping for bushing- and bearing supported pulleys and no tendon stretching on the pulley surface.

As could be observed, the friction is highly dependent on the contact angle ψ. Furthermore, zero slippage over the pulley is desired to prevent measurement errors. This may be achieved by wrapping the tendon an additional full turn around the pulley, increasing the contact area and thereby increasing static friction and preventing slippage. Note that the kinetic friction remains unchanged, as the induced additional normal forces cancel out.

F. The model of contact forces

Contact plays an essential role in gripper design. The contact modeling is defined by a finite number of contact points along the phalanges as shown in Fig. 5. The following description holds a single finger, but is identical for the other finger since symmetric. The i-th contact point is perpendicular to the surface and the i-th contact force ($F_{\text{c},i}$) is decomposed to obtain the perpendicular components w.r.t the moment arm vector as defined in Fig. 6. The perpendicular contact force component on the proximal phalange induces a torque on joint 1, while contact forces on the middle- and distal phalange induce resulting torques on both joints. The resulting induced contact torques per finger are summed to obtain the net effect ($\boldsymbol{\tau}_{\text{c}} \in \mathbb{R}^N$). For the proximal phalange, the contact torque on joint 1 ($\tau_{\text{c,proximal}\to\text{J}_1}$) is given by the i-th moment arm (M_i) times the i-th perpendicular contact force ($F_{\text{c},i}$):

$$\tau_{\text{c,proximal}\to\text{J}_1} = M_i \cos\alpha_i F_{\text{c},i}. \tag{16}$$

The expression for the middle phalange w.r.t. joint 2 ($\tau_{\text{c,middle}\to\text{J}_2}$) is similar to the proximal phalange w.r.t. joint 1.

The distal phalange is a quarter circle with origin O_{circ} as defined in Fig. 6. For the distal phalange, the i-th contact force is decomposed in the perpendicular component ($F_{i,\perp}$) of the contact force w.r.t. the moment arm. The perpendicular

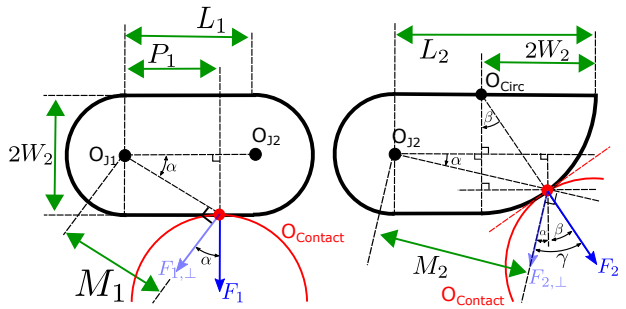

Fig. 6. Contact force decomposition. **Left:** Moment arm of proximal phalange (and middle phalange) contact point w.r.t. joint 1 (and joint 2). **Right:** Moment arm of the distal phalange contact point w.r.t joint 2.

component ($F_{i,\perp}$) is given by $F_{i,\perp} = \cos\gamma_i F_{c,i}$, where $\gamma = \alpha + \beta$. The resulting contact torque ($\tau_{c,\text{distal}\to J_2}$), is given by the moment arm (M_i) times the perpendicular force ($F_{i,\perp}$):

$$\tau_{c,\text{distal}\to J_2} = M_i \cos\gamma_i F_{c,i}. \tag{17}$$

Angle β is strictly positive, $0 \leq \beta \leq 0.5\pi$, while angle α can be positive and negative. Angle $\gamma \neq 0.5\pi$ due to geometry, so the contact torque contribution is always nonzero ($\tau_{c,\text{distal}\to J_2} > 0$).

To map the contact force present at the middle- and distal phalange to joint 1, the moment arms were defined as in Fig. 5, where distal phalange contact points are decomposed in two perpendicular forces, the length and width direction. The resulting torque induced by the distal phalange on joint 1 is given by:

$$\begin{aligned}\tau_{c,\text{distal}\to J_1} = \Big(&\cos(\beta)(P_1 + L_1\cos(q_2)) + \\ &\sin(\beta)(P_3 + L_1\sin(q_2))\Big) F_{c,i}\end{aligned} \tag{18}$$

A similar expression can be found for the the effect of a contact point on middle phalange w.r.t. joint 1 ($\tau_{c,\text{middle}\to J_1}$). The net torque ($\boldsymbol{\tau_c} \in \mathbb{R}^2$) is then given by:

$$\boldsymbol{\tau_c} = \begin{bmatrix} \tau_{c,\text{proximal}\to J_1} + \tau_{c,\text{middle}\to J_1} + \tau_{c,\text{distal}\to J_1} \\ \tau_{c,\text{middle}\to J_2} + \tau_{c,\text{distal}\to J_2} \end{bmatrix}. \tag{19}$$

G. The simulation model

The 2-DoF body is modelled using the screw theory [33] with twists, wrenches and adjoints to convert between different frames and is shown in Fig. 8. Firstly, the advantage is the easy restriction of DoFs and limiting out-of-plane movements and forces, reducing complexity. Secondly, easy extension for different finger configurations or more out-of-plane movement and forces is possible. The presented kinematic model and contact forces is limited to 2D and requires modification in case of 3D, especially the contact model.

The tendons are modeled as rigid cables with a non-linear spring in series. The friction is modeled as an modulated resistors (MR), with parameter $\eta_i(q_1)$. Transformers are used to convert forces to torques and flow sources to change length of tendon connected to one end of the non-linear spring. For modeling a rigid body the fictitious forces are disregarded because the bodies are assumed to be rotating relatively slow.

The grasp object is modeled as a sphere with a spring attached between the sphere's center of mass and the i-th contact point with (non)linear spring constant k_{object}. Object deformation is not taken into account.

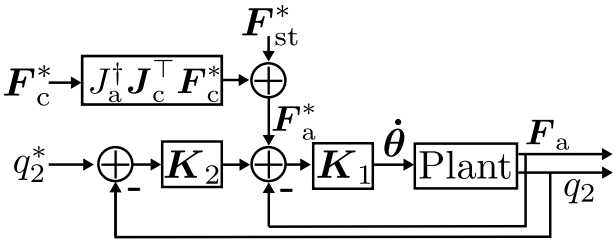

Fig. 7. The proposed control strategy. The plant is shown in Fig. 8.

IV. Control

The aim of the control strategy is to regulate contact forces at the phalanges. This is achieved using earlier defined contact and actuator jacobians, together with known elongation-force relations of the nonlinear springs. Simultaneously, co-contraction of opposing tendons can be utilized to regulate joint stiffness. Fig. 7 shows the control strategy with velocity setpoints of the motors $\dot{\boldsymbol{\theta}}$ applied to the plant.

The control strategy regulates the non-linear spring elongation based on a desired contact force. The control strategy also regulates the angle of joint 2 (q_2). This allows to regulate the angle of the contact forces, either 1) in parallel to ensure a parallel pinch with minimal reliance on friction, or 2) inward towards the gripper to move the object towards an envelope grasp.

Let C represent the number of contact points per finger. In equilibrium, torques produced by the contact forces and by actuation cancel out, i.e. $\boldsymbol{J}_t \boldsymbol{F}_a = \boldsymbol{J}_c \boldsymbol{F}_c$, where $\boldsymbol{J}_c$ denotes the contact Jacobian and $\boldsymbol{F}_c$ denotes contact forces. Rewritten, a desired contact force, $\boldsymbol{F}^*_c \in \mathbb{R}^C$, can be used to obtain actuator setpoints, $\boldsymbol{F}^*_a \in \mathbb{R}^A$. Increasing joint stiffness is achieved by increasing all the non-linear spring forces equally. Therefore, $\boldsymbol{F}_a$ is given by the summation of the desired contact force and stiffness component ($\boldsymbol{F}_{st}$):

$$\boldsymbol{F}^*_a = J_t^\dagger \boldsymbol{J}_c^\top \boldsymbol{F}^*_c + \boldsymbol{F}_{st}, \tag{20}$$

where $\boldsymbol{J}_t^\dagger := \left(\boldsymbol{J}_t^\top \boldsymbol{J}_t\right)^{-1} \boldsymbol{J}_t^\top$ denotes the Moore-Penrose pseudo inverse of $\boldsymbol{J}_t$, since $\boldsymbol{J}_t$ can be non-square. For simplicity, only the most dominant contact points per phalange are used, $C = 2$. The pseudo-inverse can be calculated once since it contains only constant joint radii.

Note that the plant includes the conversion between measured states (non-linear spring deflections and angular actuator positions) and control variables ($\boldsymbol{F}_a$ and q_2) as well as low-level control loops for motor velocity control. $\boldsymbol{F}_a$ is calculated using Eq. (7) and the measured non-linear spring deflections. The non-linear spring deflections are controlled in a inner loop with proportional gain, $\boldsymbol{K}_1 = \text{diag}(K_{p1}, K_{p1}, K_{p1})$.

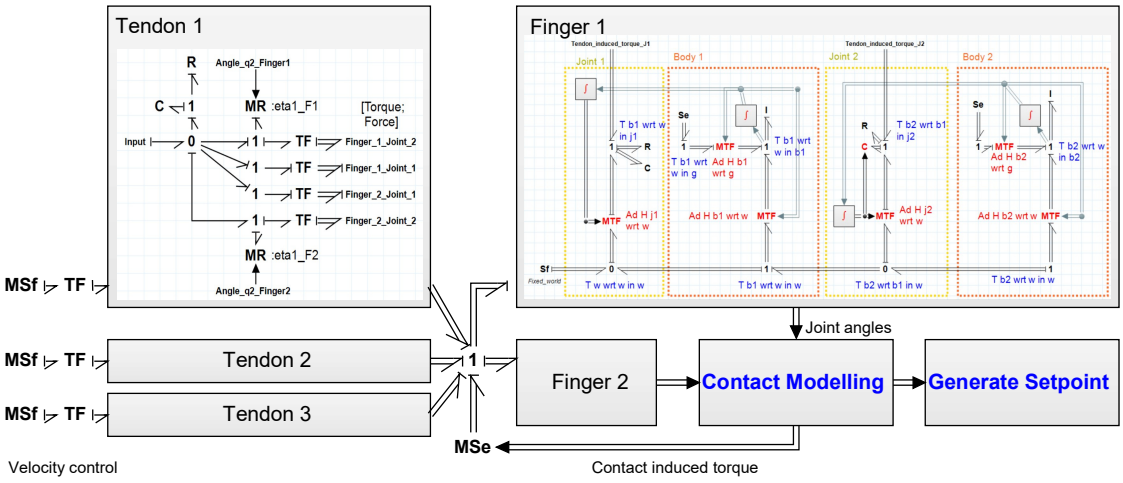

Fig. 8. Simplified bond graph model of gripper.

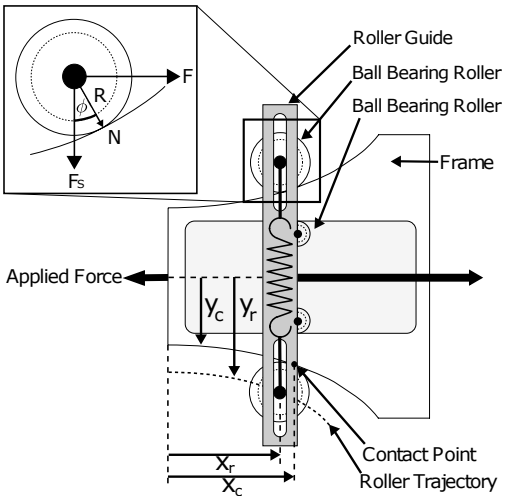

Fig. 9. Cam-follower description of non-linear spring based on [22].

An outer loop is used to control the joint 2 angle (q_2), using $\boldsymbol{K_2} = \text{diag}(K_{\text{p2}}, -K_{\text{p2}}, 0)$. The control priority is set to regulate the non-linear spring forces, so K_{p1} and K_{p2} are selected to ensure $\boldsymbol{K}_1\boldsymbol{e}_1 > \boldsymbol{K}_2\boldsymbol{e}_2$, where $\boldsymbol{e}_1$ and $\boldsymbol{e}_2$ denotes the errors, respectively.

The grasp type, envelope or pinch grasping, is actively determined by setting the desired contact forces (in combination with q_2). Zero desired contact force at the proximal phalange results in a pinch grasp and a non-zero desired contact force on all phalanges results in an envelope grasp.

V. Non-linear spring implementation

The non-linear spring requires a specific quadratic force-displacement relation. The most easily tunable method with the highest load capacity is a cam-follower, although its size is significant and has higher friction compared to the earlier mentioned (adapted) triangle and four-bar mechanisms. We choose the cam-follower as the proof-of-concept for its ease of implementation. To obtain the force-displacement relation, we follow the concept and solution proposed by [22].

The cam-follower design of Fig. 9 stretches a roller guide relative to a specific frame contour, while the ball bearings are connected via two linear springs (one on either side of the frame). The applied force-deflection relationship is dependent on the contour shape. The independent variable, x_{r}, is the horizontal distance from the left-most edge of the frame to the rollers' center point, such that $x_{\text{r}} \geq 0$. x_{c} is the horizontal distance to the rollers' contact point and other relationships found are given by:

$$\begin{aligned} x_{\text{c}} &= x_{\text{r}} + R\sin\phi \\ \text{F}\left(x_{\text{r}}\right) &= N\sin\left(\phi\left(x_{\text{r}}\right)\right) \\ \text{F}_{\text{s}}\left(x_{\text{r}}\right) &= N\cos\left(\phi\left(x_{\text{r}}\right)\right) \\ \frac{\text{F}\left(x_{\text{r}}\right)}{\text{F}_{\text{s}}\left(x_{\text{r}}\right)} &= \tan\left(\phi\left(x_{\text{r}}\right)\right) = \text{y}_{\text{c}}'\left(x_{\text{c}}\right) \\ \text{y}_{\text{r}}\left(x_{\text{r}}\right) &= \text{y}_{\text{c}}\left(x_{\text{c}}\right) + R\cos\left(\phi\left(x_{\text{r}}\right)\right) \end{aligned} \tag{21}$$

where R is the radius of the rollers and ϕ is the angle between the rollers' normal force vectors (N) and the vertical axis. $\text{F}(x)$ is one-half of the overall force-length relationship of the device because force is transmitted equally through both rollers. $\text{F}_{\text{s}}\left(x_{\text{r}}\right)$ defines the sum of the forces exerted by both springs:

$$\text{F}_{\text{s}}\left(x_{\text{r}}\right) = 4k\left[\text{y}_{\text{r}}\left(x_r\right) - \frac{x_0}{2}\right] + F_{\text{p}} \tag{22}$$

Combining Eq. (21) and Eq. (22), the device contour, $\text{y}_{\text{c}}(x_{\text{r}})$, is given by the differential equation[1]:

$$\begin{aligned} &\text{y}_{\text{c}}{}'\left(x_c\right)\left[\text{y}_{\text{c}}\left(x_c\right) + \frac{R}{\sqrt{1+\text{y}_{\text{c}}{}'\left(x_c\right)^2}} - \frac{x_0}{2} + \frac{F_{\text{p}}}{4k}\right] - \\ &\frac{a}{8k}\left[x_c - R\left(\frac{\text{y}_{\text{c}}{}'\left(x_c\right)}{\sqrt{1+\text{y}_{\text{c}}{}'\left(x_c\right)^2}}\right)\right]^2 - \frac{c}{8k} = 0. \end{aligned} \tag{23}$$

[1]Corrected equation from contribution of [22]. In Eq. (22), $x_0 \rightarrow \frac{x_0}{2}$ and in Eq. (23) $\text{y}_{\text{c}}{}'\left(x_{\text{c}}\right)^2\left(\frac{F_{\text{p}}}{4k}\right) \rightarrow \text{y}_{\text{c}}{}'\left(x_{\text{c}}\right)\left(\frac{F_{\text{p}}}{4k}\right)$.

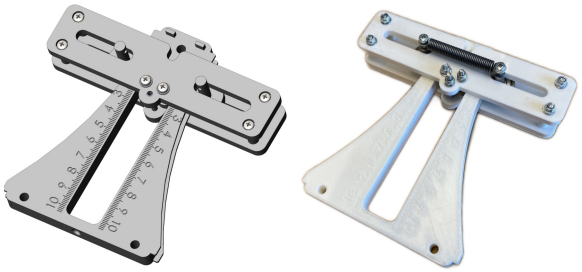

Fig. 10. Non-linear spring. **Left:** CAD model. **Right:** 3D printed prototype.

Numerical solutions to Eq. (23) are computed using Mathematica 13, using equation parameters: k = 11.8 N/cm, x_0 = 4.9 cm, F_p = 22.6 N, R = 0.79 cm, c = 1 N and a = 2 or 4 N/cm^2. The parameters are selected for the available components and to have a significant deflection range (of several cm), which reduces measurement errors/noise and limits the non-ideal behaviour of the linear springs. To prevent the roller guide from acting as a whippletree, additional (small) bearings are located on the roller guide on the inside trajectory with an offset in x-direction w.r.t. the center of the ball bearing. Size could be drastically decreased while maintaining the force-deflection curve, by increasing e.g. linear spring stiffness (k) or decreasing roller guide radius (R), but at the cost of increased non-idealities. Fig. 10 shows the CAD model and 3D printed proof-of-concept. Fig. 11 shows the force-deflection curves of three manufactured prototypes, together with a second-order fit and the desired curve. All devices demonstrate strong correlation to desired quadratic behavior (r^2 = 0.9940, 0.9896, and 0.9845, respectively). The actuation of the device's roller guide is in discretized displacement steps, which is visible as a stick-slip behavior in the individual runs.

VI. Prototype

The prototype of Fig. 12 contains two compact fingers on top and the non-linear springs, differential mechanism and actuators located in the wrist. Rigidity is ensured by aluminum square profiles connected to a thick (Delrin) top and bottom plate with adjustable spacing. Flange bushings (Igus) enables low rotational friction in the 2-DoF body in a compact fitting. Similarly, the pulleys inside the phalange are plastic bushing-supported. The tendon guidance in the base/wrist contains four bearing-guided pulleys for each tendon with constant wrapping angle of 0.25π rad. The tendons are actuated using Dynamixel MX64 servo motors. All angles are measured using AMS AS5048A magnetic position sensors. The geometric parameters are listed in Table I. The selected values ensure possible pinch grasping, and 5-point stability envelope grasping for the earlier specified object diameter range.

The design choices determine the torque-deflection relations of both joints. Fig. 13 shows the torque-deflection relations for co-contraction of counteracting tendons with different tendon tensile forces (of 10 to 110 N in steps of 25 N) in simulation. Joint friction between phalanges is neglected to obtain intuitive torque-deflection relations without hysteresis. The resulted stiffness ranges for joint 1 and 2 are 0.46-1.39 Nm/rad and

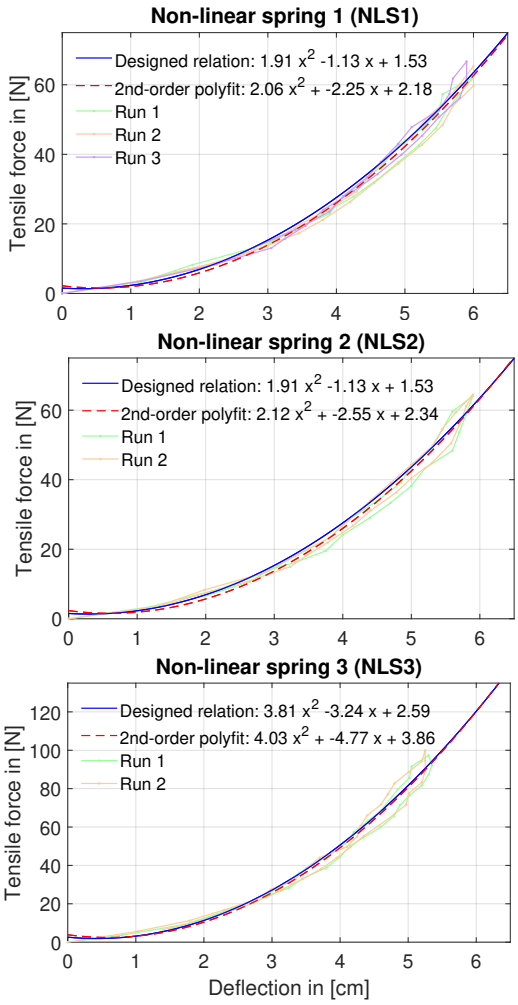

Fig. 11. Characterization of the force-displacement relation of the fabricated non-linear springs.

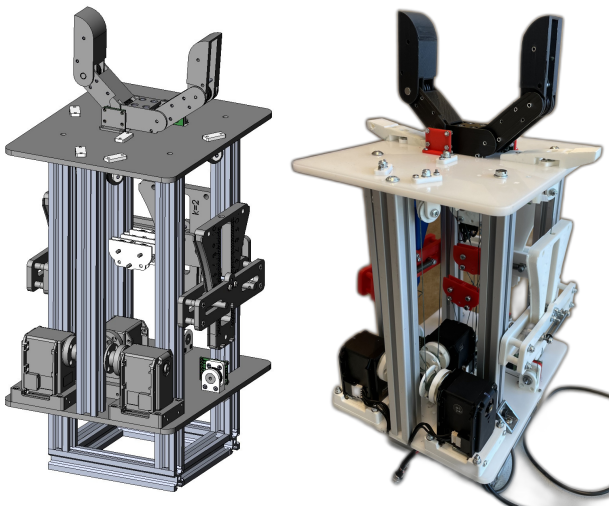

Fig. 12. Proof-of-concept **Left:** CAD model. **Right:** Fabricated prototype.

TABLE I
PARAMETERS IN PROTOTYPE.

Parameter		Value	Unit
Actuator radius	r_a	7.5	mm
Joint radii	r_1, r_2	7.5	mm
Length base	L_0	40.0	mm
Length phalanges	L_1, L_2	47.5	mm
Width phalanges	W_1, W_2, W_3	10.0	mm

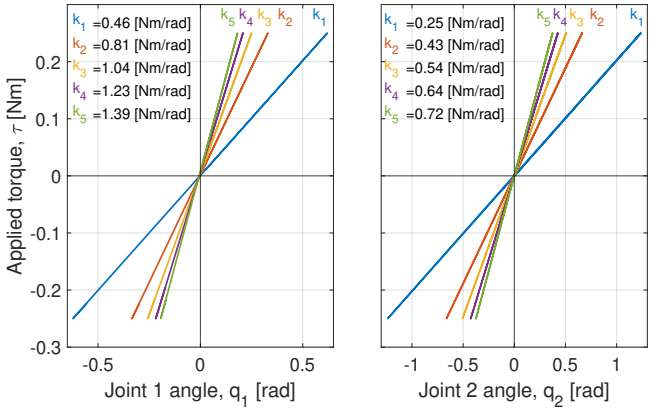

Fig. 13. Characterization of the torque deflection curve of joint 1, q_1

0.25-0.72 Nm/rad, respectively. The stiffness ratio between joint 1 and joint 2 is approximately a factor of 2 (1.84-1.93), which is in line with earlier derived Eq. (11) where k_1 has all k_2 terms doubled with an additional term dependent on q_1.

VII. RESULTS

Multiple experiments are used to validate the prototype and the attractive features. These are listed and elaborated below.

1) Joint 2 state estimating using remote sensing
2) Friction loss of tensile force in tendon chain
3) Torque-deflection relation for joint 2
4) Stiffening of joint 2
5) Grasping a variety of objects

Firstly, the validity of the remote joint 2 angle sensing is tested, including the absolute error of joint 2 for different tensile forces. Secondly, the tensile force at different positions of the tendon chain is measured to analyze friction losses. Next, the stiffness range of joint 2 is compared between the prototype and theoretical design. To check if an object can be grasped and stiffness can be increased without increasing contact force, a pinch grasp is performed on a cylindrical object and afterwards tendons co-contract. Lastly, to validate performance, a grasp visualization of a deformable cylinder in simulation and prototype is shown, together with additional grasp visualizations of a variety of different objects in size and stiffness.

A. Experiment 1: Joint 2 state estimating using remote sensing

To test the remote sensing validity, the joint 2 estimation accuracy is tested for multiple tensile forces with an additional

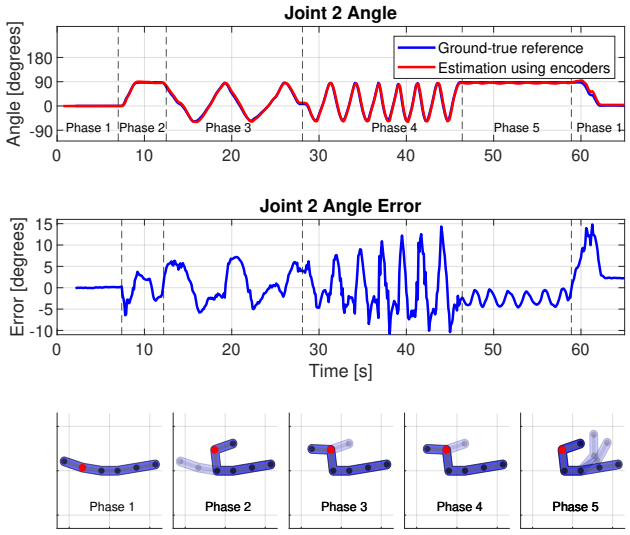

Fig. 14. Results experiment 1: Joint 2 estimation of single finger using encoders. Tendon 1 has a constant tensile force of 40 N, other tendons are slack. **Top:** Angle range and phase indicating. **Middle:** Corresponding error. **Bottom:** Phase visualisation. Remotely sensed joint is marked red. Phase 1: initial state. Phase 2: Moving only measurement finger to both joint limits. Phase 3: Slowly move only measurement J2 in full range. Phase 4: Significant faster movement of only measurement J2 in full range. Phase 5: Place measurement finger at joint limit and move other finger.

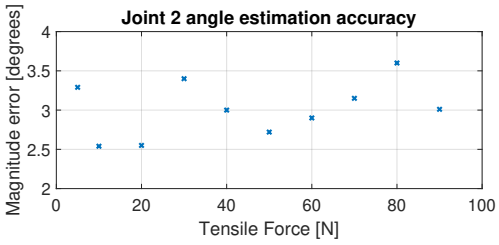

Fig. 15. Results experiment 1: Accuracy of joint 2 estimation for different tensile forces. Experiment is based on a single run of each phase with a equal duration of 10 seconds and approximately the same movement speed.

position sensor on joint 2 as a ground-true reference. The accuracy is tested in 5 different phases, with varying movement speeds and joint angle states. The phases are emphasized in Fig. 14. The error is in the range of $\pm$ 5 degrees for slow movements (phase 3) and in the range of $\pm$ 10 degrees for faster movements (phase 4). Movement of the other finger (phase 5) results in a error significantly smaller than for phases 3 and 4. The experiment is repeated while varying the tensile force, with the absolute angle estimation error shown in Fig. 15. Each single run consisted of each phase with a equal duration of 10 seconds and approximately the same movement speed. No trend can be observed and an overall average of about 3 degrees is observed for all tensile forces.

B. Experiment 2: Friction loss of tensile force in tendon chain

To measure friction losses, the tensile force over the tendon is measured in four locations, 1) after the non-linear spring, 2) after two bearing guided pulleys with 'single winded' wrapping angle of 0.5π rad, 3) after two bearing guided pulleys with 'double winded' wrapping angle of 2.5π rad and 4) the

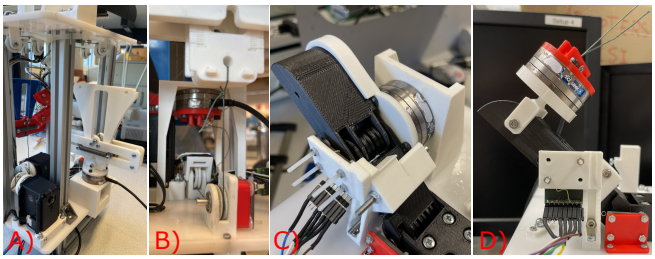

Fig. 16. Measurement setup. **(A)** Tensile force measurement directly after non-linear spring. **(B)** Tensile force measurement after two routing pulleys. **(C)** Induced torque measurement. **(D)** Torque-deflection measurement.

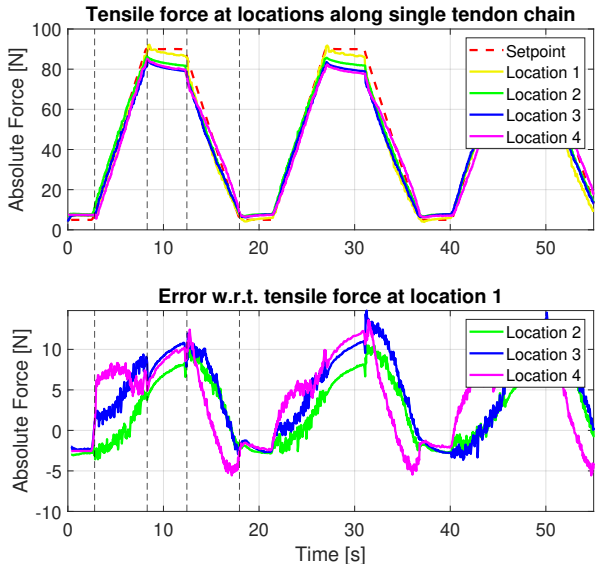

Fig. 17. Results experiment 2: Cumulative friction losses along single tendon routing.

converted torque to tensile force at joint 2. Fig. 16 shows the measurement setup. Testing is done using an ATI Industrial Mini-40 force-torque sensor as a ground-truth reference connected on both sides with a 3D printed bracket to a tendon. The actuators drive the non-linear spring continuously between initial deflection and a deflection corresponding to a tensile force of 90 N. At both deflections, the actuators are shortly paused. The result for a single actuator and non-linear spring is shown in Fig. 17. The error is larger for an increased number of routing points and increased winding angle.

It can be observed that the intended tensile force by the springs is partially present at the gripper's joints due to cumulative friction losses along the tendon routing. The force routing efficiencies (defined in Section III-E) w.r.t. non-linear spring tensile force for positions 2, 3 and 4 are respectively $\eta_2 = 0.72$, $\eta_3 = 0.61$ and $\eta_4 = 0.54$ for 20 N and up to $\eta_2 = 0.95$, $\eta_3 = 0.92$ and $\eta_4 = 0.90$ for 90 N. Although the single- and double-winded pulleys should have the same efficiency according to Eq. (15), the value of η_3 is slightly lower than η_2. This may be caused by the neglected effect of friction arising from a tendon moving past itself in the same v-groove for a double-winded pulley.

Fig. 17 shows a relaxing behaviour with tendon tension

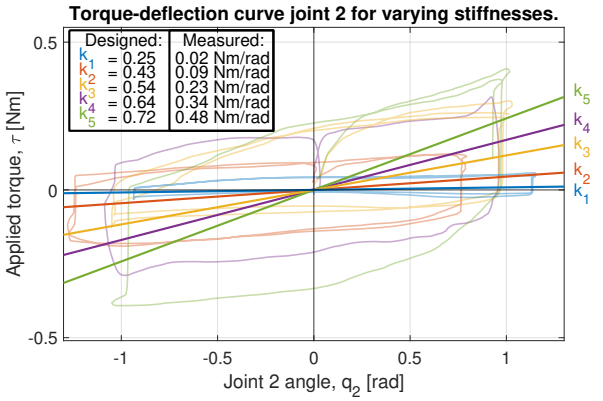

Fig. 18. Results experiment 3: Characterization of the torque deflection curve of joint 2 (q_2).

decreasing when the actuators are paused (e.g. between 9 and 12 s). When paused, the actuators were barely moving, since the measured tensile force using encoders in the software had reached the setpoint with neglectable error. The behaviour is common for viscoelastic materials like polymers. [34].

C. Experiment 3: Torque-deflection relation for joint 2

The torque-deflection relation range is measured in the prototype to check correspondence with designed range. Joint 1 is fixed using a 3D printed bracket and torque is applied by pulling on a tendon, while the force is measured using the ATI-40 force sensor. Fig. 16d shows the measurement setup. The stiffness is increased by linearly increasing all elements of $\boldsymbol{F}_{\text{st}}$ in Eq. (20) from 10 to 110 N in steps of 25 N. Fig. 18 shows the torque-deflection relations together with first-order fits. An increasing stiffness results in a larger hysteresis. The first-order fit indicates a significant error between the stiffness range in simulation and prototype. Both show a linearly increased stiffness, which is in line with Eq. (11). The average error between simulation and prototype is 0.284 Nm/rad (61.7%) with range 0.23-0.31 Nm/rad (33.3-92.0%).

D. Experiment 4: Stiffening of joint 2

To test the stiffness feature on an deformable object, a grasp is performed with a certain contact force setpoint of 10 N. The stiffness is increased by applying a ramp-function with finite start (t=15 s) and stop time (t=25 s) as shown in Fig. 19. During the experiment, the theoretical stiffness value is calculated using Eq. (11).

The simulation shows a contact force in equilibrium equal to the setpoint, also while stiffening. The prototype shows a lower equilibrium of 7.08 N (29.2 % error). During stiffening, the grasp force deviates around $\pm$ 0.65 N (9.2 %). The prototype shows an slight increase in joint angle (closing motion of gripper) in the first seconds of stiffening.

E. Experiment 5: Grasping different and off-center objects

A grasp of a 50 mm diameter deformable cylinder with stiffness of 120 N/m is compared in simulation and prototype

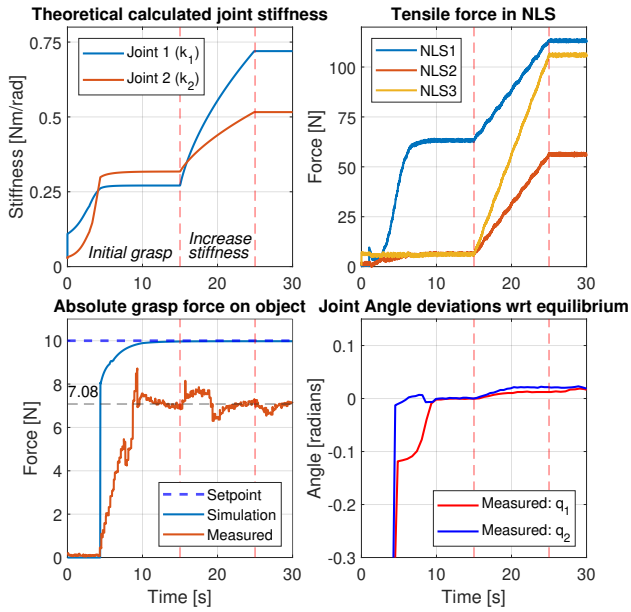

Fig. 19. Results experiment 4: Stiffening joint 2. Equilibrium grasp position is reached at t = 15 s, afterwards stiffness is increased by co-contraction, visible in top-right figure. **Top:** Theoretical joint stiffness and induced tendon tensile force by the the non-linear springs. **Bottom:** Absolute grasp force applied on object and deviation of the joint 2 angle w.r.t. grasp equilibrium.

in Fig. 20. It can be seen than the finger remains straight for longer, although the end position is very similar. In simulation the the object is a little more squeezed, following from the reduced contact force due to friction losses. Note that the simulation does not shown the object deformation, but only overlap between the fingers and object.

Fig. 21 shows a practical grasp collection with various objects of different size, shape, stiffness, and mass. Objects were also rotated and placed off-center. It can be observed that the gripper has established successful grasps for this wide range.

VIII. Discussion

The discussion on results and observations are summarized in a few points below.

A. Imperfections of non-linear springs

When considering the non-linear spring prototypes, the discretized behavior in Fig. 11 could be caused by 3D printed imperfections in combination with high forces in the linear springs. When the rollers are having a nonzero velocity, the effect is reduced compared to a close to zero-velocity (e.g. for small deviations around setpoint). A device printed in ABS and cleaned with alcohol to smooth out the path could reduce the effect even further.

It is important to have an exact zero-deflection point on the devices, since small deflection errors result in significant force errors at large deflections. Additionally, the assumption of infinitely rigid bodies and non-stretching tendons does not hold. For higher tensile forces in the tendons, the (Delrin) plates starts bending and knots are tightened further. The improved clinch knot was used, which tightens when tensile force is applied. Also, the tendon stretches, although a very stiff multiple stranded polyethylene fiber fish line was used. To reduce stretching, a small diameter metal cable is favorable, but the flexibility should be sufficient to wrap inside the tight spaces, knotting is more difficult and sliding friction would increase. The non-constant tendon length in combination with a variable zero-deflection point complicates balancing a tensile force between two opposing tendons. Therefore, when increasing joint stiffness, the joint angle shifts and the magnitude contact force increases as observed in Fig. 19.

B. Proof-of-concept rigidity

3D printing is well suited for fabricating complex shapes and light-weighted parts, but it remains plastic, which deforms relatively easily compared to steel. Identically, the plastic bearings used as bushing-supported bearings in the phalanges rotate freely under small loads, but for increased loads, the friction increased significantly. This is visible in the torque-deflection curves of joint 2 in Fig. 18, causing significant hysteresis. Overall, the friction losses in the tendon routing and bearing/bushing-supported pulleys resulted in the smaller tensile forces present in the tendon chain in Fig. 17 and magnitude error in Fig. 19.

When comparing Figs. 17 to 19, the obtained stiffness errors (33.3-92.0%) are larger than the tensile force errors (10.0-46.0%) and magnitude contact error (29.2%). In Fig. 17, the phalanges are barely moving by experimental setup constraints, while in Fig. 18, the distal phalange moves in the full range of joint 2. Therefore, the friction between phalanges and joints is much more dominant in Fig. 18. The error in Fig. 19 is in line with the previous statement since a low tensile is applied in the phase to obtain a grasp equilibrium and while increasing joint 2 stiffness, the phalanges barely move. Replacement using metal-bearing supported pulleys could reduce effects. A different filament like ABS or carbon fiber could reduce the problem as well.

C. Design iteration induced weaknesses

Design iterations of gripper parts induced misalignments between actuators, tendon-routing points and differential mechanisms. For example, the differential mechanism tendon output to be non-parallel to the tendon inlet at the base (angle difference of about 7 degrees). Therefore, Eq. (13), describing the estimation of the joint 2 angle using remote sensing and assuming a parallel configuration, does not hold.

The material deflection and tendons stretch are the main causes of the error in joint 2 angle estimation of Fig. 14. An increased error could be observed for fast movements compared to slow movements. The increased error for faster movement is due to the errors induced in the spring deflection measurement, since the encoder measurement is delayed by one cycle (sample time = 32.4 ms) plus the delay in low-level control loop for motor velocity control. However, the error decreases when the motion was slowed down or paused for a short period. Other control types could deal with this problem, but the goal was to keep the control simple and including

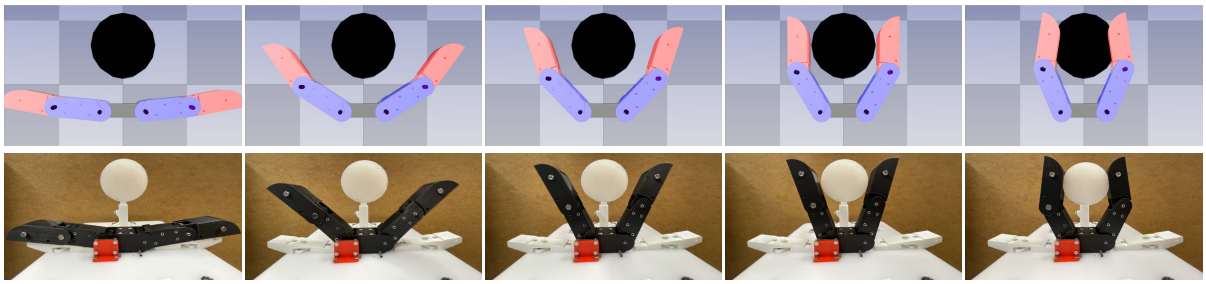

Fig. 20. Grasping of 50 mm diameter cylinder made out of ECOFLEX 20 with stiffness of about 120 N/m.

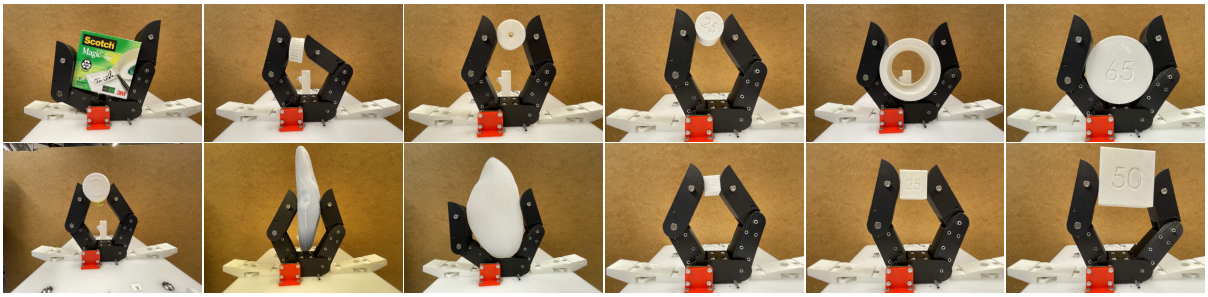

Fig. 21. Practical grasp cases. The diameter or width is visualized in mm on the 3D printed items as a reference.

e.g. derivative terms are not desired since velocities are commanded. For slow movement, the desired spring deflection is maintained by the controller without any problem. A more detailed analysis is required since layered control loops are interacting. The error for slow movement can be explained by the earlier stated problems, e.g. the tendon not being a solid link, but slightly stretchable, not perfectly round printed pulleys (not infinitely stiff) and plastic deflection. All these effects accumulate into the error of ± 5 degrees in Fig. 14. The variation around the mean value of about 3 degrees could be explained by the small differences in the time duration of phases.

D. Adaptability feature

The adaptability feature is viable in a limited range, determined by geometry. If joint angles are within limits, the feature maintains a stable grasp while moving the object or external forces are applied. When one of the joint limits is hit, the object looses contact and falls out of the gripper.

IX. Conclusion

The concept of a gripper based on multiple tendons in an agonist-antagonist setup has been proven to be viable. The developed simulation model illustrates the attractive benefits of the gripper and provides a valuable tool for both simulation and development. The proof-of-concept prototype also showed these attractive benefits in experiments, such as the ability to grasp objects with high compliance and afterwards increase stiffness to make acceleration possible and to increase grasp stability. Also, the design showed adaptability to alignment issues and irregular shapes when approaching objects or external applied forces. The gripper includes three non-linear springs with designed force-deflection relations. Reducing the number of sensors and locating the sensors for the second joint angle remotely reduces possible contact and increases cleanability.

In future work, it would be beneficial to improve the proof-of-concept mechanical structure by replacing (3D printed) plastic components suffering from force deformation by stiffer materials. Frictional effects in the gripper and routing should be reduced. A further analysis of the layer control structure is necessary. In terms of applicability, the wrist size should be minimized, starting by minimizing the size of the non-linear springs. By using stiffer and stronger materials, the total dimensions can be reduced, while maintaining attractive benefits of the gripper.

Acknowledgment

Firstly, I would like to thank dr.ir. W. Roozing for his continued feedback and excellent guidance during the thesis process. His experience has helped to guide the research more effectively and his critical thinking always provided useful feedback.

Secondly, the technical staff at the RAM department of the University of Twente, in particular Q. Sable, for their generous feedback and help in practical considerations of the construction and manufacturing.

References

[1] L. Wang and H. Zhang, "An adaptive fuzzy hierarchical control for maintaining solar greenhouse temperature," *Computers and Electronics in Agriculture*, vol. 155, pp. 251–256, 6 2018.

[2] B. Zhang, Y. Xie, J. Zhou, K. Wang, and Z. Zhang, "State-of-the-art robotic grippers, grasping and control strategies, as well as their applications in agricultural robots: A review," *Computers and Electronics in Agriculture*, vol. 177, p. 105694, 10 2020.

[3] D. Ireri, E. Belal, C. Okinda, N. Makange, and C. Ji, "A computer vision system for defect discrimination and grading in tomatoes using machine learning and image processing," *Artificial Intelligence in Agriculture*, vol. 2, pp. 28–37, 6 2019.

[4] NWO/TTW, "FlexCRAFT Project," 2022. [Online]. Available: https://flexcraftprogram.com/

[5] W. Crooks, G. Vukasin, M. O'Sullivan, W. Messner, and C. Rogers, "Fin Ray effect inspired soft robotic gripper: From the robosoft grand challenge toward optimization," *Frontiers Robotics AI*, vol. 3, no. NOV, p. 70, 11 2016.

[6] Y. Gao, X. Huang, I. S. Mann, and H. J. Su, "A Novel Variable Stiffness Compliant Robotic Gripper Based on Layer Jamming," *Journal of Mechanisms and Robotics*, vol. 12, 2020.

[7] M. Ciocarlie, F. M. Hicks, R. Holmberg, J. Hawke, M. Schlicht, J. Gee, S. Stanford, and R. Bahadur, "The Velo gripper: A versatile single-actuator design for enveloping, parallel and fingertip grasps," *The International Journal of Robotics Research*, vol. 33, pp. 753–767, 2014.

[8] A. M. Dollar and R. D. Howe, "The SDM Hand: A Highly Adaptive Compliant Grasper for Unstructured Environments," *Springer Tracts in Advanced Robotics*, vol. 54, pp. 3–11, 2009.

[9] H. Dong, E. Asadi, C. Qiu, J. Dai, and I.-M. Chen, "Geometric design optimization of an under-actuated tendon-driven robotic gripper," *Robotics and Computer-Integrated Manufacturing*, vol. 50, pp. 80–89, 2017. [Online]. Available: www.elsevier.com/locate/rcim

[10] C. Rossi and S. Savino, "An Underactuated Multi-finger Grasping Device:," *International Journal of Advanced Robotic Systems*, vol. 11, 6 2014.

[11] I. Hussain, M. Malvezzi, D. Gan, Z. Iqbal, L. Seneviratne, D. Prattichizzo, and F. Renda, "Compliant gripper design, prototyping, and modeling using screw theory formulation," *International Journal of Robotics Research*, vol. 40, pp. 55–71, 6 2021.

[12] S. Shirafuji, S. Ikemoto, and K. Hosoda, "Tendon routing resolving inverse kinematics for variable stiffness joint," *IEEE International Conference on Intelligent Robots and Systems*, pp. 3886–3891, 2014.

[13] R. J. Anderson, "Advanced dexterous manipulation for IED defeat : report on the feasibility of using the ShadowHand for remote operations." Sandia National Laboratories (SNL), Albuquerque, NM, and Livermore, CA (United States), Tech. Rep., 1 2011.

[14] Z. Ren, N. Kashiri, C. Zhou, and N. G. Tsagarakis, "HERI II: A Robust and Flexible Robotic Hand based on Modular Finger design and Under Actuation Principles," *IEEE International Conference on Intelligent Robots and Systems*, pp. 1449–1455, 6 2018.

[15] M. G. Catalano, G. Grioli, E. Farnioli, A. Serio, C. Piazza, and A. Bicchi, "Adaptive synergies for the design and control of the Pisa/IIT SoftHand:," *http://dx.doi.org/10.1177/0278364913518998*, vol. 33, pp. 768–782, 2014.

[16] M. Santello, M. Bianchi, M. Gabiccini, E. Ricciardi, G. Salvietti, D. Prattichizzo, M. Ernst, A. Moscatelli, H. Jörntell, A. M. L. Kappers, K. Kyriakopoulos, A. Albu-Schäffer, C. Castellini, A. Bicchi, and M. Santello, "Hand synergies: Integration of robotics and neuroscience for understanding the control of biological and artificial hands HHS Public Access," *Phys Life Rev*, vol. 17, pp. 1–23, 2016.

[17] B. Vanderborght, A. Albu-Schaeffer, A. Bicchi, E. Burdet, D. G. Caldwell, R. Carloni, M. Catalano, O. Eiberger, W. Friedl, G. Ganesh, M. Garabini, M. Grebenstein, G. Grioli, S. Haddadin, H. Hoppner, A. Jafari, M. Laffranchi, D. Lefeber, F. Petit, S. Stramigioli, N. Tsagarakis, M. Van Damme, R. Van Ham, L. C. Visser, and S. Wolf, "Variable impedance actuators: A review," *Robotics and Autonomous Systems*, vol. 61, pp. 1601–1614, 6 2013.

[18] S. S. Groothuis, G. Rusticelli, A. Zucchelli, S. Stramigioli, and R. Carloni, "The variable stiffness actuator vsaUT-II: Mechanical design, modeling, and identification," *IEEE/ASME Transactions on Mechatronics*, vol. 19, pp. 589–597, 2014.

[19] S. Kawamura, T. Yamamoto, D. Ishida, T. Ogata, Y. Nakayama, O. Tabata, and S. Sugiyama, "Development of passive elements with variable mechanical impedance for wearable robots," *Proceedings - IEEE International Conference on Robotics and Automation*, vol. 1, pp. 248–253, 2002.

[20] J. Choi, S. Hong, W. Lee, S. Kang, and M. Kim, "A robot joint with variable stiffness using leaf springs," *IEEE Transactions on Robotics*, vol. 27, no. 2, pp. 229–238, 4 2011.

[21] V. R. Ham, T. G. Sugar, B. Vanderborght, K. W. Hollander, and D. Lefeber, "Compliant actuator designs: Review of actuators with passive adjustable compliance/controllable stiffness for robotic applications," *IEEE Robotics and Automation Magazine*, vol. 16, pp. 81–94, 2009.

[22] S. A. Migliore, E. A. Brown, and S. P. DeWeerth, "Biologically inspired joint stiffness control," *Proceedings - IEEE International Conference on Robotics and Automation*, vol. 2005, pp. 4508–4513, 2005.

[23] N. Vitiello, C. M. Oddo, T. Lenzi, S. Roccella, L. Beccai, F. Vecchi, M. C. Carrozza, and P. Dario, "Neuro-robotics paradigm for intelligent assistive technologies," *Springer Tracts in Advanced Robotics*, vol. 106, 2015.

[24] S. Ayyasamy, P. Ramu, S. K. Gurunathan, and S. Bandyopadhyay, "Design of a Four-bar mechanism to guide the motion of a falling tube," *IPRoMM 2016*, 6 2016.

[25] M. R. Cutkosky and P. K. Wright, "MODELLING MANUFACTURING GRIPS AND CORRELATIONS WITH THE DESIGN OF ROBOTIC HANDS." *IEEE International Conference on Robotics and Automation (ICRA)*, pp. 1533–1539, 1986.

[26] M. R. Cutkosky, "On Grasp Choice, Grasp Models, and the Design of Hands for Manufacturing Tasks," *IEEE Transactions on Robotics and Automation*, vol. 5, no. 3, pp. 269–279, 1989.

[27] R. Ozawa, H. Kobayashi, and K. Hashirii, "Analysis, classification, and design of tendon-driven mechanisms," *IEEE Transactions on Robotics*, vol. 30, pp. 396–410, 2014.

[28] A. B. Clark, L. Liow, and N. Rojas, "Force evaluation of tendon routing for underactuated grasping," *Journal of Mechanical Design, Transactions of the ASME*, vol. 143, no. 10, 10 2021.

[29] L. Birglen and C. M. Gosselin, "Force Analysis of Connected Differential Mechanisms: Application to Grasping:," *http://dx.doi.org/10.1177/0278364906068942*, vol. 25, no. 10, pp. 1033–1046, 7 2016. [Online]. Available: https://journals.sagepub.com/doi/10.1177/0278364906068942

[30] R. M. Raymond, U. O. Lael, A. Dollar, and L. Odhner, "A Modular, Open-Source 3D Printed Underactuated Hand," *2013 IEEE International Conference on Robotics and Automation (ICRA)*, 2013.

[31] R. Cabás, L. M. Cabas, and C. Balaguer, "Optimized design of the underactuated robotic hand," *Proceedings - IEEE International Conference on Robotics and Automation*, vol. 2006, pp. 982–987, 2006.

[32] Y. Peng, Y. Wei, and M. Zhou, "Efficient modeling of cable-pulley system with friction based on arbitrary-Lagrangian-Eulerian approach," *Applied Mathematics and Mechanics*, vol. 38, pp. 1785–1802, 2017. [Online]. Available: https://doi.org/10.1007/s10483-017-2284-8

[33] J. M. Selig, "Applying screw theory to robot dynamics," *Journal of Applied Mathematics and Mechanics*, pp. 159–167, 1991.

[34] W. N. W. N. Findley, J. S. Lai, and K. Onaran, "Nonlinear Creep at Constant Stress and Relaxation at Constant Strain," in *Creep And Relaxation Of Nonlinear Viscoelastic Materials With An Introduction To Linear Viscoelasticity*, ser. North-Holland series in applied mathematics and mechanics ; v. 18. North-Holland Pub. Co., 1976, vol. 18, pp. 176–219.

4 Additional findings

During the thesis, some interesting findings or extra clarification results were obtained. The most interesting findings are elaborated below.

4.1 Non-linear spring relation solutions

The non-linear spring contours are the solution of the earlier specified differential equation in the paper. There is not a unique solution to the differential equation, as shown on the left in Fig. 4.1. The selected contact path has a second-order poly-fit. There is a significant offset between both solutions. However, there is little difference between the obtained force-deflection relations shown on the right side, despite the large offset in the contour. The contact path's slope is similarly for both solutions after a 2 cm deflection. It can be observed that in y', there is a large peak at the start, but both solutions diverge to the same value. For multiple tested desired relations, this difference is present. Solution 1 is selected since it is intuitively more logical. Considering time, solution 2 is not manufactured to check whether this is a valuable solution or not.

Solution 1 was fabricated using 100% infill PLA with a thickness of 10 mm. The rollers used are 1) inner diameter: 3mm, outer diameter 10 mm and 2) inner diameter: 6mm, outer diameter 19 mm. In case of lack of strength, carbon fiber could be printed to increase strength but turned out to be not essential. For a minimized redesign, this could be beneficial. The force by the linear spring is stated as usual (deflection of 4 cm) as: 140 N and maximum (at 8 cm deflection) as 233 N. These values double for the spring with double stiffness, at the bottom of Fig. 4.1.

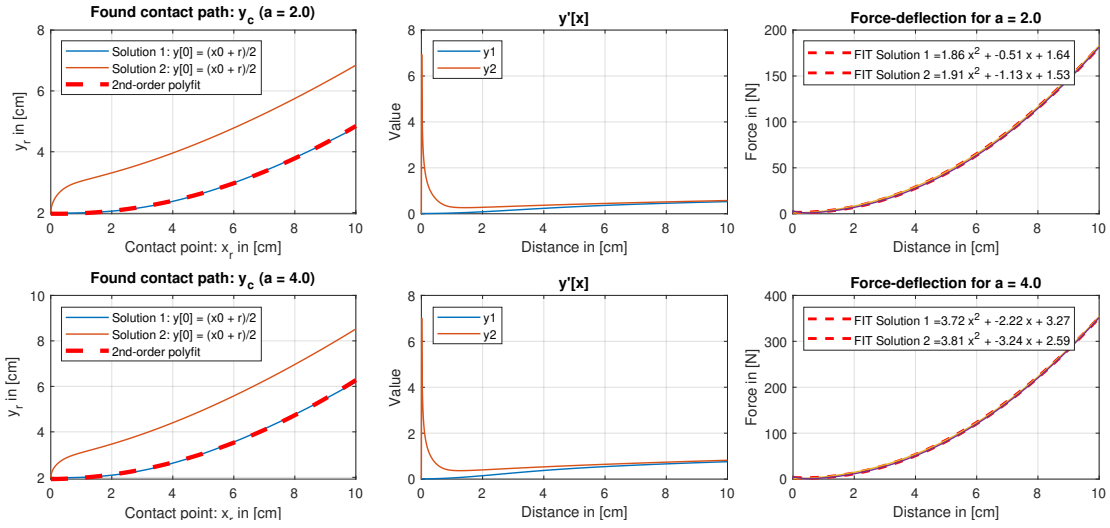

Figure 4.1: Solution to the differential equation in the paper. **Top row:** Solution for Non-linear spring 1 and 2(NLS1 & NLS2). Both are identical since both have identical desired force-deflection relations. **Bottom row:** Solution for non-linear spring 3 (NLS3). The difference is the quadratic slope constant (a), which is doubled for NLS3 wrt NLS1 & NLS2. **Left column:** Obtained contact path. **Middle column:** Obtained derivative of contact path. **Right column:** Force-deflection relation from obtained contact path.

4.2 Stiffening effect in simulation

The effects of increasing stiffness of joint 2 in the simulation are shown in more detail in Fig. 4.2. Again, an initial grasp is performed and after 10 s, the joint stiffness is increased by co-contraction. The non-linear spring deflections, angular position and non-linear spring force are shown for each pair of actuator and tendon. The non-linear spring force increases linearly (bottom line of Fig. 4.2), while the tendon state and angular actuator position change depending on the current deflection position of the non-linear spring.

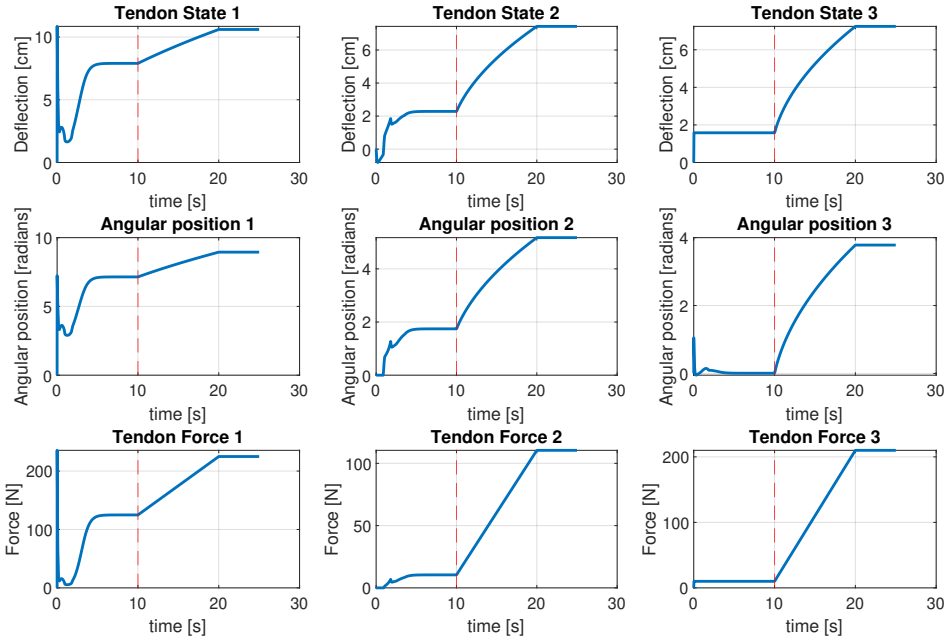

Figure 4.2: Effects of increasing stiffness of joint 2 in simulation. Each column represents a subgroup containing a single tendon, actuator and non-linear spring. The red dotted line indicates the start of co-contraction.

4.3 Torque-deflection relations (individual)

The individual plots of torque-deflection relations of the paper are plotted for clarity below in Fig. 4.3.

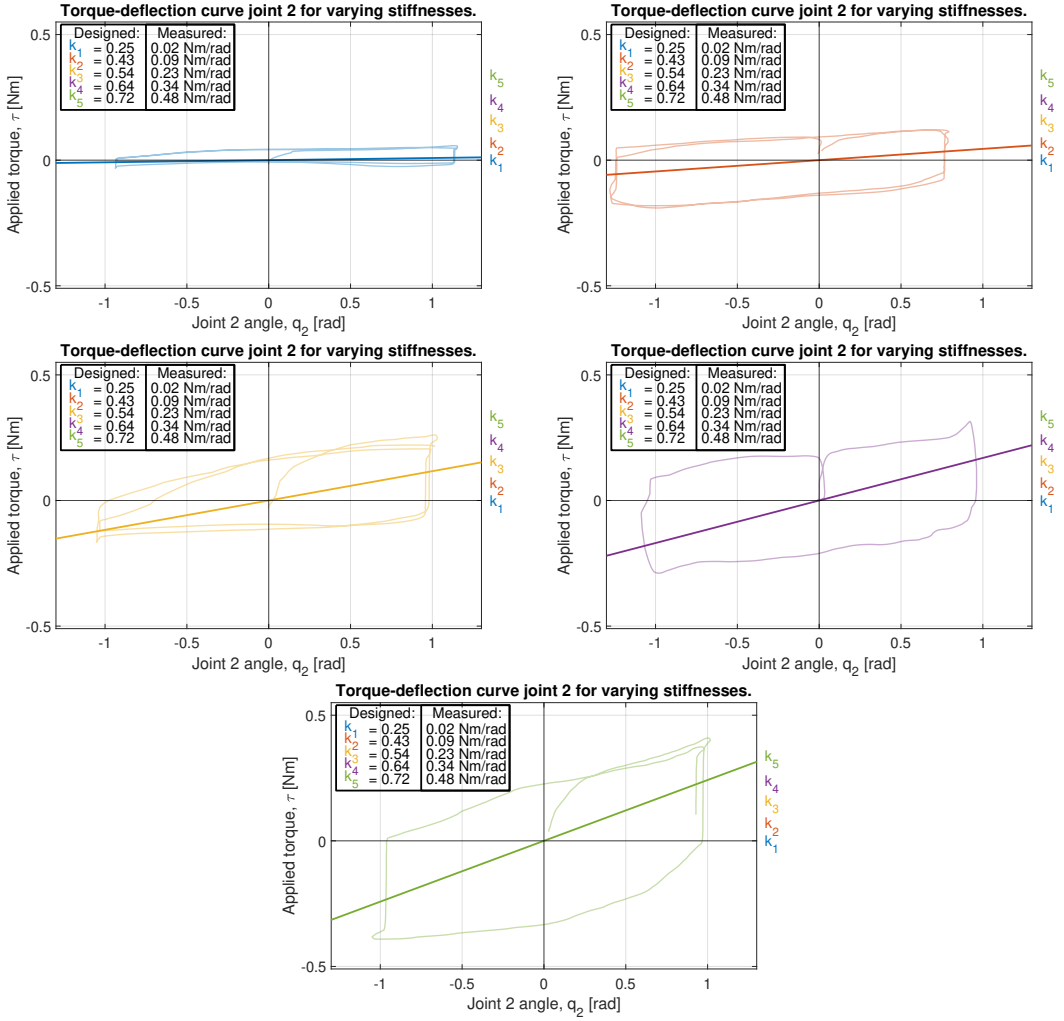

Figure 4.3: Individual characterizations of the torque deflection curve of joint 2.

5 Design Iterations

Between the initial design and the final design, several designed parts are iterated, aiming to improve the gripper behaviour and performance. The most significant design iterations are elaborated below.

5.1 Non-linear springs

The initial designed non-linear springs suffered from the wheel carrier acting as a whipple-three. The adapted design includes additional small bearings in an inner contour with a fixed offset distance to the rolling bearings. Also, the rollers moved out-of-plane w.r.t. the contour due to small misalignments and non-identical linear springs. Therefore, the design is adapted by printing guidance rails for the rolling bearings, increasing sliding friction between the guidance and rolling bearing. The initial design had a limited force-deflection range, which range was simply increased by extending the contour, as in Fig. 5.1. The force-deflection relation was measured using a bucket, which was filled with water. Water was added in portions of about 500 mL, weighted before added.

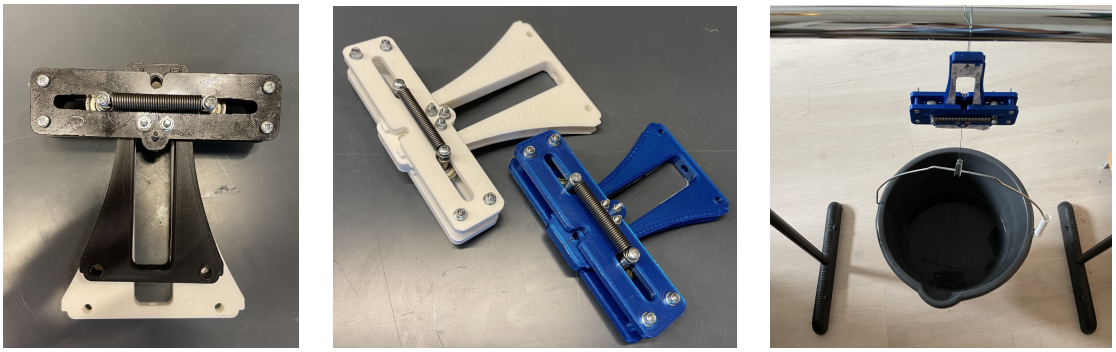

Figure 5.1: Design iteration non-linear springs. **Left:** Increasing range of force-deflection relation. **Middle:** Adding guidance rails on contour. **Right:** Experimental setup for measuring force-deflection relations.

5.2 Limited actuator power

The initially required maximum torque in simulation turned out to be 1 N.m. The Dynamixel XC-430-W150-T was selected, since 1.6 N.m initially seemed to be sufficient. However, they got easily overheated since they are only rated to work shortly at their high-range torque and could only work for a longer time (> 2 min) at 40% of their capacity. Therefore, the actuators are replaced by Dynamixel MX64, which delivers 6.0 N.m. However, the dimensions are larger, so the initial three-on-a-row structure (see Fig. 5.2) is not feasible. The three-on-a-row structure took benefit from minimal deflection since the (Delrin) plate is supported on both sides by an aluminium square profile. The actuators are re-positioned inside the possible space, which resulted in misalignment between the actuator and the first routing point inlet. The tensile force goes up to 100 N, which is a point where (5mm thick Delrin) plates start deflecting (next to tendon stretching), which induced significant measurement errors. The deflection is made visible with the red line in Fig. 5.2. Replacement with steel plates would reduce this side-effect, but was not implemented considering time.

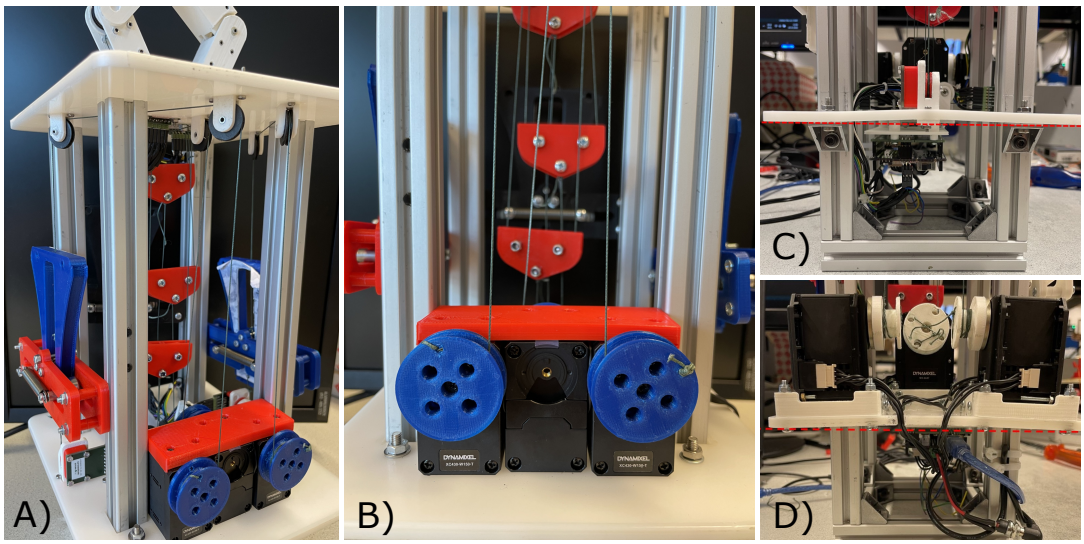

Figure 5.2: Actuator placement. **A,B:** Initial actuators aligned with tendon routing pulleys. **C,D:** Location of more powerful actuators. Also, indicating plate deflection of maximum load on both sides.

5.3 Tendon routing frictional losses

The tendon routing contained two types of guidance, a pulley with and without an encoder.

5.3.1 Tendon routing without encoder

The tendon routing pulley without an encoder is only used to redirect the tendon direction to keep the gripper compact. The main weaknesses are illustrated in Fig. 5.3. One of the main weaknesses of the initial design was the tendon going out of the v-groove in the pulley, resulting in a huge increase in sliding friction. Additionally, due to misalignment by implementing stronger actuators, the tensile force was no longer perpendicular to the pulley's rolling axis. Consequently, the guidance increased significant friction by clamping the pulley's side faces with the guidance. The initial design had Teflon pulleys rotating as a bushing-supported pulley around an aluminium bar. All these weaknesses are improved by implementing a ball-bearing-supported pulley with sufficient spacing between pulley side faces and outer guidance. Also, the guidance pulley is connected to the Delrin plate via a bolt and nut making it rotatable and adjustable to small alignment errors. Also, the whole guidance was printed under a slight angle to capture the expected misalignment.

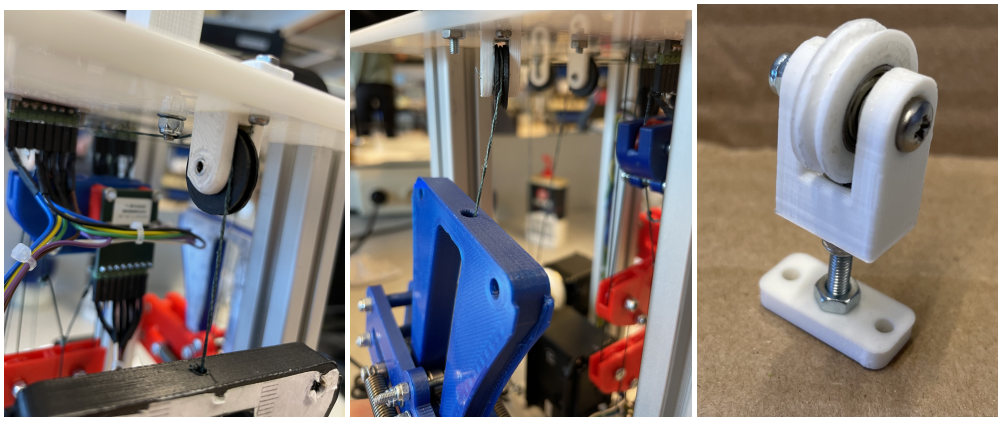

Figure 5.3: Tendon routing without encoder. **Left:** Tendon running out of the v-groove increasing slipping friction. **Middle:** Tendon not perpendicular to dominant motion axis resulting in the clamping between pulley and guidance. **Right:** Bearing-supported guidance with adjustable orientation.

5.3.2 Tendon routing with encoder

The integrated actuator encoder and one encoder-pulley are used to obtain the force-deflection of a single non-linear spring. The tendon guidance with an integrated encoder was designed slightly different compared pulley without an integrated encoder since the rotational angle of the pulley should be measured. The guidance is shown in Fig. 5.4. A magnet is connected to an aluminium shaft with a 3D printed adapter. The shaft is press-fit through the pulley's center and supported on both sides by ball-bearings. The pulley guidance with encoder had the same weaknesses as the pulley guidance with encoder. Additionally, the tendon should not unwind, since it would result in measurement errors. As described in the paper, therefore, the double-winded structure is proposed to increase the contact area, at cost of increased friction.

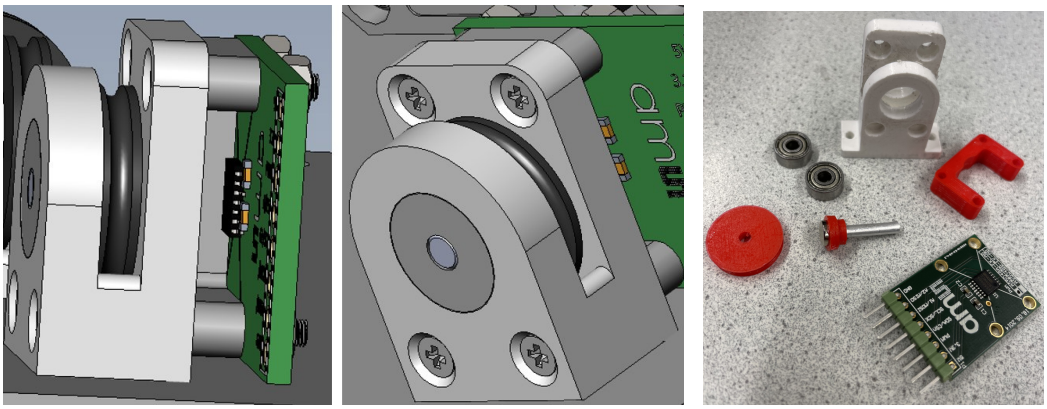

Figure 5.4: Tendon routing with integrated encoder. **Left & Middle:** CAD model of initial design. **Right:** 3D printed iterated design.

The tendon routing in the differential mechanism is shown in Fig. 5.5. It contains on the left of a blue pulley on both sides supported by bearings and on the right side with a bearing inside the red pulley. Both are different, since, on one pulley, an encoder needs to be attached, which requires the pulley to move together with the axle. The other side of the differential mechanism is connected to both bolts via a small tendon.

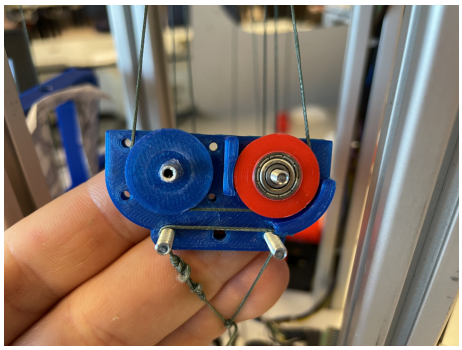

Figure 5.5: Prototype of differential mechanism with implemented encoder.

The gripper is shown in Fig. 5.6. The phalanges were connected via plastic bushings (IGUS inc., 2022) and an aluminium rod to have low friction in the desired rotational direction and high friction in both other perpendicular directions. Aluminium rods of 2 mm diameter were selected to minimize contact surface and minimize gripper weight while preventing deformation under radial load. Initially, the pulleys were printed in nylon with the aluminum rods acting as bushing supports. The pulleys start tilting in the direction of the rotation axis, causing the pulleys to get stuck (clamp) and increased sliding friction. The effects were reduced by sup-

porting the pulleys on both sides with plastic bushings (as bottom-right in Fig. 5.6). For low tensile forces, this was sufficient, but low friction couldn't be ensured when large tensile forces are applied. The phalanges were 3D printed are designed for compactness with less accent on rigidity, since positioning multiple pulleys and routing pins inside the body was complex. Therefore, the desired restriction of the phalanges to rotate around a single axis does not apply. For further design, this is something to keep in mind.

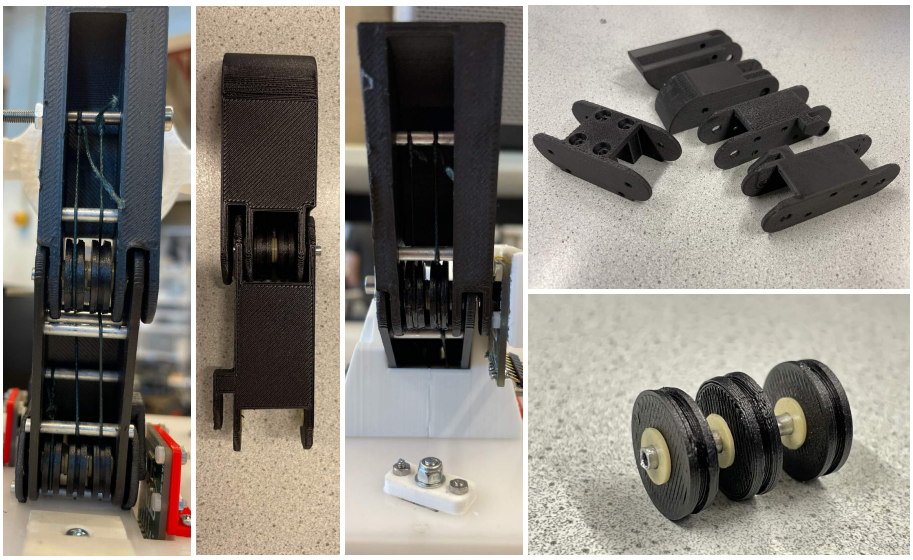

Figure 5.6: Prototype of 2DoF finger.

5.4 Controller implementation

The controller is implemented using an Arduino Uno with a Dynamixel shield. The three actuators are connected via TTL running firmware version 1. The shield blocked the method to update the firmware of the Dynamixel MX64 to version 2, which offered much more compact and elegant function descriptions. The Arduino runs with a cycle time of about 32.4 ms, which determines the update rate of the setpoint generator and encoder functions. A total of 6 encoders are connected via SPI to minimize wiring. The encoders wrap each 2π, so a function is implemented to get cumulative angles. The Arduino code can be found in the supplementary material.

6 Simulation model

The paper mentions shortly the most important contributions of the simulation model, which are elaborated in more detail below.

The modeling of the 2DOF body per finger is done using the screw theory with twists, wrenches and adjoints to convert between different frames. Some more details about screw theory can be found in Selig (1991) and in Appendix A. The modeling software 20Sim is used and an overview of the model is shown in Fig. 6.1. The 20sim file is added as supplementary material. Each rigid body is described as a 1-junction to which an I-type element is connected. This method is used because, in the initial stage, the DoF can be easily restricted to reduce the complexity, and also because, in an advanced stage, it can be used to include out of plane compliance or disturbances. Adding a third finger positioned an z-offset above the other fingers is relatively easy, but requires an adapted contact modeling, since currently object can only move and rotate within plane and tiling is not possible.

As stated before, the tendons are modeled as rigid cables with a non-linear spring in series. The frictional losses are modeled as an modulated resistors (MR), with parameter $\eta(q_1)$. The wrapping efficiency is modeled, but stick-slip frictional losses were not characterized (and thus not included) for the bushing-supported phalanges and bushing-supported pulleys. Transformers are used to convert forces to torques and actuatiors as flow sources moving one spring end of the tendon chain, while the other end was fixed to the distal phalange. For modeling a rigid body, the fictitious forces are disregarded because the bodies are assumed to be rotating relatively slow. The effect of gravitational forces on the pulleys, tendons and springs are neglectable, but gravity of the phalanges is included.

The contact modeling is visualized in Fig. 6.1 as *"Obstacles"*. It utilizes the joint states (H-matrices) of both fingers to calculate a tensile force setpoint according to the method shown in the paper, which is the output of *"GenerateSetpoint"*. The contact model could be extended as accurate as possible, but this research is restricted to a couple of contact points. The object is modeled as a sphere with a spring attached between the sphere's center and the i-th contact point. In this way, varying the stiffness, fully rigid to compliance objects can be simulated and the forces exerted on the object can be visualized. The object's position and orientation is visualized by applying in the netto external forces on an independent body. Many deformable objects have an increasing stiffness-deflection curve, since the object density increases when squeezed. Therefore, the force in the contact spring is modeled as $F(x) = a(x - x_0)^2 + b(x - x_0)$.

The effects of the contact are modulated by calculating the distance between the contact point and joints, to calculate the moment arm and contact angle (angle between phalange and object), which is always rectangular. The spring deformation is multiplied with the spring constant to obtain the reaction force, which is multiplied with the moment arm to obtain the resulting torque. This torque is fed back using an modulated effort source (MSe) into the individual joints.

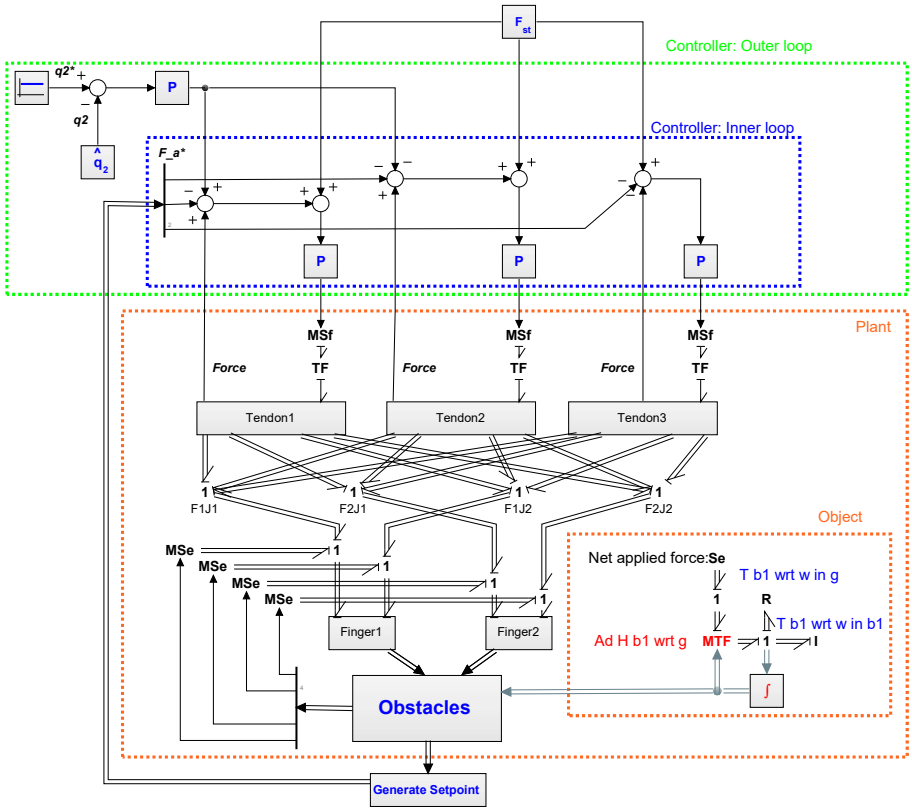

(a) Full model.

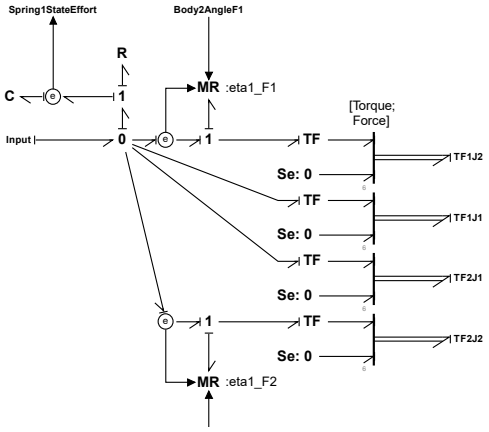

(b) Submodel Tendon.

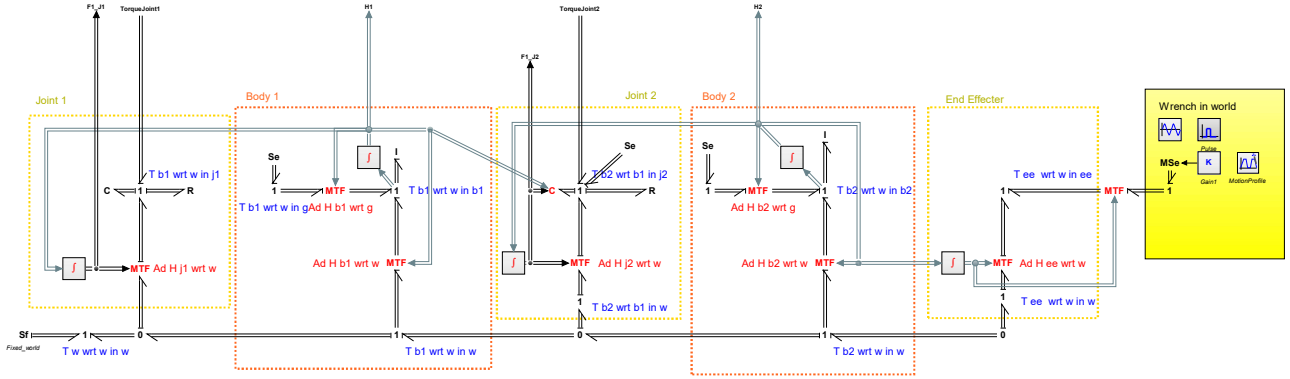

(c) Submodel Finger.

Figure 6.1: Model in 20sim. Fullmodel, submodel tendon and submodel finger.

7 Conclusion

The main conclusions of the research have already been given in the core paper (Chapter 3), therefore this section will focus on the conclusions with respect to the requirements stated in the other chapters.

All requirements stated in the MoSCoW for the 'must have' and 'should have' are satisfied. Additionally, the remote sensing of joint 2 in 'could have' is also implemented. Mechanically design optimization is (partly) included in the tendon routing guidance and outer casing, to aim for a rigid and compact gripper design. Despite this, further optimization is required. The other requirements under 'could have' are not included considering time and impact on other characteristics. The requirements for 'won't have' are not included by default. The obtained contact force ranges from 0 - 7.08 N and the stiffness range 0.02 - 0.48 Nm/rad. Note that the specified contact force range is the range whereafter the joint stiffness could be increased by a factor of 3. The maximum grasp force limit is exceeding, but stiffness could not be increased afterward. Multiple available objects were grasped successfully, where the maximum object mass was a cylinder (made out of ECOFLEX 20) of 400 g.

An overview of the desired requirements of design and the proof-of-concept is shown in Table 7.1.

Table 7.1: Overview of initial quantifiable design requirements and fabricated gripper.

Parameter	**Desired amount**	**Proof-of-concept**	**Unit**
Contact grasp force	0.71 - 14.66	0 - 7.08	N
Stiffness range (joint 2)	??	0.02 - 0.48	Nm/rad
Maximum object mass	≥ 200	≥ 400	g

A Screw Theory

A n-dof finger can be modeled using the screw theory. For general velocities in 3-D, there are 6 degrees of freedom: 3 rotations and 3 translations. A twist is a "6-D" velocity that can be expressed as a 6×1 vector. A simple and intuitive way to construct the Twist is to append linear velocity to angular velocity.

$$T = \begin{pmatrix} \omega \\ v \end{pmatrix} \tag{A.1}$$

Note the dependency of the frames. The twist ${}^{c}\boldsymbol{T}_{a}^{b}$ is represented as: *"T of a wrt b in c"*

Velocities, twists, are vectors. An operator that acts on a vector and yields a (scalar) real number, is called a co-vector. Since power is calculated as $P = F \cdot v, F$ must be a co-vector: it is an operator on velocity and yields a real number. For each velocity vector, whether it be linear velocity v, rotational velocity ω, or a twist T, there is a dual force-like co-vector: F, τ, and the wrench W.

$$P = WT = \begin{pmatrix} \tau & F \end{pmatrix} \begin{pmatrix} \omega \\ v \end{pmatrix} \tag{A.2}$$

We write W as a row-vector to indicate that it is a co-vector.

One point in frame A can be expressed in frame B,

$${}^{A}p = R_{B}^{A}\,{}^{B}p + {}^{A}O_{B} \Leftrightarrow {}^{A}P = \begin{bmatrix} R_{B}^{A} & {}^{A}O_{B} \\ 0 & 1 \end{bmatrix} {}^{B}P$$

where the new matrix is called the homogeneous matrix or H-matrix:

$$H_{B}^{A} := \begin{bmatrix} R_{B}^{A} & {}^{A}\mathrm{O}_{B} \\ 0 & 1 \end{bmatrix}.$$

Twist can be transformed between frames using the Adjoint matrix. The twist of an body body or frame with respect to another body or frame expressed in A can be expressed in B by mapping of the Adjoint matrix of H_{A}^{B},

$${}^{B}T_{\bullet}^{\bullet} = Ad_{H_{A}^{B}}\,{}^{A}T_{\bullet}^{\bullet}, \tag{A.3}$$

where $Ad_{H_{A}^{B}}$ is given by:

$$Ad_{H_{A}^{B}} = \begin{bmatrix} R_{A}^{B} & 0 \\ {}^{B}\tilde{o}_{A}R_{A}^{B} & R_{A}^{B} \end{bmatrix}, \tag{A.4}$$

where ${}^{B}\tilde{o}_{A}$ is the skew symmetric matrix. The skew symmetric matrix is defined as:

$$x = \begin{pmatrix} x_1 \\ x_2 \\ x_3 \end{pmatrix} \Rightarrow \tilde{x} = \begin{pmatrix} 0 & -x_3 & x_2 \\ x_3 & 0 & -x_1 \\ -x_2 & x_1 & 0 \end{pmatrix} \tag{A.5}$$

Each rigid body is described as a **1**-junction to which a **I**-type element is connected.

A rigid body expressed in body-fixed frame is denotes as Ψ_k. The 1-junction represents the Twist, or velocity in all 6 dimensions, of the body, with respect to the world-fixed frame Ψ_0 expressed in body-fixed frame Ψ_k. Further, the **I**-type element contains the body's inertia matrix

expressed in body-fixed frame as:

$$ {}^{k}\mathscr{I} = \begin{bmatrix} I_{xx} & 0 & 0 & 0 & 0 & 0 \\ 0 & I_{yy} & 0 & 0 & 0 & 0 \\ 0 & 0 & I_{zz} & 0 & 0 & 0 \\ 0 & 0 & 0 & m & 0 & 0 \\ 0 & 0 & 0 & 0 & m & 0 \\ 0 & 0 & 0 & 0 & 0 & m \end{bmatrix} \tag{A.6} $$

The constitutive equations of the **I**-type element are

$$ \begin{aligned} {}^{k}\dot{\mathscr{P}}^{\mathrm{T}} &= {}^{k}W^{\mathrm{T}} \\ {}^{k}\mathscr{T}_{k}^{0} &= {}^{k}\mathscr{I}^{-1} \cdot {}^{k}\mathscr{P}^{\mathrm{T}} \end{aligned} \tag{A.7} $$

Here, ${}^{k}\mathscr{P}$ is the state of the **I** element.

Only when twists are expressed with respect to the same reference frame can they be added or subtracted. Therefore, **MTFs** are required to transform between different reference frames. These **MTFs** contain the specific homogeneous matrix (H-matrix) describing the transformation between the two frames, more precisely: the rotational as well as translational transformation.

Bibliography

Anderson, R. J. (2011), Advanced dexterous manipulation for IED defeat : report on the feasibility of using the ShadowHand for remote operations., Technical report, Sandia National Laboratories (SNL), Albuquerque, NM, and Livermore, CA (United States), doi:10.2172/1011226.

Catalano, M. G., G. Grioli, E. Farnioli, A. Serio, C. Piazza and A. Bicchi (2014), Adaptive synergies for the design and control of the Pisa/IIT SoftHand:, *http://dx.doi.org/10.1177/0278364913518998*, **vol. 33**, pp. 768–782, ISSN 17413176, doi:10.1177/0278364913518998.

Ciocarlie, M., F. M. Hicks, R. Holmberg, J. Hawke, M. Schlicht, J. Gee, S. Stanford and R. Bahadur (2014), The Velo gripper: A versatile single-actuator design for enveloping, parallel and fingertip grasps, *The International Journal of Robotics Research*, **vol. 33**, pp. 753–767, doi:10.1177/0278364913519148.

Cutkosky, M. R. and P. K. Wright (1986), MODELLING MANUFACTURING GRIPS AND CORRELATIONS WITH THE DESIGN OF ROBOTIC HANDS., *IEEE International Conference on Robotics and Automation (ICRA)*, pp. 1533–1539, doi:10.1109/ROBOT.1986.1087525.

Dollar, A. M. and R. D. Howe (2009), The SDM Hand: A Highly Adaptive Compliant Grasper for Unstructured Environments, *Springer Tracts in Advanced Robotics*, **vol. 54**, pp. 3–11, doi:10.1007/978-3-642-00196-3{_}2.

Dong, H., E. Asadi, C. Qiu, J. Dai and I.-M. Chen (2017), Geometric design optimization of an under-actuated tendon-driven robotic gripper, *Robotics and Computer-Integrated Manufacturing*, **vol. 50**, pp. 80–89, doi:10.1016/j.rcim.2017.09.012.
www.elsevier.com/locate/rcim

Gao, Y., X. Huang, I. S. Mann and H. J. Su (2020), A Novel Variable Stiffness Compliant Robotic Gripper Based on Layer Jamming, *Journal of Mechanisms and Robotics*, **vol. 12**, ISSN 19424310, doi:10.1115/1.4047156/1083603.

Hussain, I., M. Malvezzi, D. Gan, Z. Iqbal, L. Seneviratne, D. Prattichizzo and F. Renda (2021), Compliant gripper design, prototyping, and modeling using screw theory formulation, *International Journal of Robotics Research*, **vol. 40**, pp. 55–71, ISSN 17413176, doi:10.1177/0278364920947818.

IGUS inc. (2022), IGUS Flange Bearings.
https://www.igus.com/info/flange-bearing

NWO/TTW (2022), FlexCRAFT Project.
https://flexcraftprogram.com/

Ren, Z., N. Kashiri, C. Zhou and N. G. Tsagarakis (2018), HERI II: A Robust and Flexible Robotic Hand based on Modular Finger design and Under Actuation Principles, *IEEE International Conference on Intelligent Robots and Systems*, pp. 1449–1455, ISSN 21530866, doi:10.1109/IROS.2018.8594507.

Rossi, C. and S. Savino (2014), An Underactuated Multi-finger Grasping Device:, *International Journal of Advanced Robotic Systems*, **vol. 11**, doi:10.5772/57419.

Sam, R. and S. Nefti (2010), Design and feasibility tests of multi-functional gripper for handling variable shape of food products, *Conference Proceedings - IEEE International Conference on Systems, Man and Cybernetics*, pp. 1267–1272, ISSN 1062922X, doi:10.1109/ICSMC.2010.5642431.

Selig, J. M. (1991), Applying screw theory to robot dynamics, *Journal of Applied Mathematics and Mechanics*, pp. 159–167.

Starke, J., K. Chatzilygeroudis, A. Billard and T. Asfour (2019), On Force Synergies in Human Grasping Behavior, doi:10.0/Linux-x86{_}64.

Tlegenov, Y., K. Telegenov and A. Shintemirov (2014), An open-source 3D printed underactuated robotic gripper, *MESA 2014 - 10th IEEE/ASME International Conference on Mechatronic and Embedded Systems and Applications, Conference Proceedings*, doi:10.1109/MESA.2014.6935605.

Tsugami, Y., T. Barbie, K. Tadakuma and T. Nishida (2018), Development of universal parallel gripper using reformed magnetorheological fluid, *2017 Asian Control Conference, ASCC 2017*, **vol. 2018-January**, pp. 778–783, doi:10.1109/ASCC.2017.8287269. https://tohoku.pure.elsevier.com/ja/publications/development-of-universal-parallel-gripper-using-reformed-magnetor

Ultimaker (2022), Ultimaker S5. https://ultimaker.com/3d-printers/ultimaker-s5

Wang, L. and H. Zhang (2018), An adaptive fuzzy hierarchical control for maintaining solar greenhouse temperature, *Computers and Electronics in Agriculture*, **vol. 155**, pp. 251–256, ISSN 0168-1699, doi:10.1016/J.COMPAG.2018.10.023.

Zhang, B., Y. Xie, J. Zhou, K. Wang and Z. Zhang (2020), State-of-the-art robotic grippers, grasping and control strategies, as well as their applications in agricultural robots: A review, *Computers and Electronics in Agriculture*, **vol. 177**, p. 105694, ISSN 0168-1699, doi:10.1016/J.COMPAG.2020.105694.